



The KMOS^{3D} Survey: Rotating Compact Star-forming Galaxies and the Decomposition of Integrated Line Widths*

E. Wisnioski^{1,2,3}, J. T. Mendel^{1,2,3}, N. M. Förster Schreiber¹, R. Genzel^{1,4}, D. Wilman^{1,5}, S. Wuyts⁶, S. Belli¹, A. Beifiori^{1,5}, R. Bender^{1,5}, G. Brammer⁷, J. Chan⁸, R. I. Davies¹, R. L. Davies¹, M. Fabricius¹, M. Fossati^{1,5}, A. Galametz¹, P. Lang⁹, D. Lutz¹, E. J. Nelson¹, I. Momcheva⁷, D. Rosario¹⁰, R. Saglia¹, L. J. Tacconi¹, K. Tadaki¹¹, H. Übler¹, and P. G. van Dokkum¹²

¹ Max-Planck-Institut für extraterrestrische Physik (MPE), Giessenbachstr. 1, D-85748 Garching, Germany; emily.wisnioski@anu.edu.au

² Research School of Astronomy and Astrophysics, Australian National University, Canberra, ACT 2611, Australia

³ ARC Centre for Excellence in All-Sky Astrophysics in 3D (ASTRO 3D), Australia

⁴ Departments of Physics and Astronomy, University of California, Berkeley, CA 94720, USA

⁵ Universitäts-Sternwarte, Ludwig-Maximilians-Universität, Scheinerstrasse 1, D-81679 München, Germany

⁶ Department of Physics, University of Bath, Claverton Down, Bath, BA2 7AY, UK

⁷ Space Telescope Science Institute, 3700 San Martin Drive, Baltimore, MD 21218, USA

⁸ Department of Physics and Astronomy, University of California, Riverside, CA 92521, USA

⁹ Max-Planck-Institut für Astronomie, Königstuhl 17, D-69117 Heidelberg, Germany

¹⁰ Center for Extragalactic Astronomy, Department of Physics, Durham University, South Road, Durham, DH1 3LE, UK

¹¹ National Astronomical Observatory of Japan, 2-21-1 Osawa, Mitaka, Tokyo 181-8588, Japan

¹² Astronomy Department, Yale University, New Haven, CT 06511, USA

Received 2017 November 2; revised 2018 January 24; accepted 2018 February 16; published 2018 March 12

Abstract

Using integral field spectroscopy, we investigate the kinematic properties of 35 massive centrally dense and compact star-forming galaxies (SFGs; $\log \bar{M}_* [M_\odot] = 11.1$, $\log(\Sigma_{\text{H}\alpha} [M_\odot \text{ kpc}^{-2}]) > 9.5$, $\log(M_*/r_e^{1.5} [M_\odot \text{ kpc}^{-1.5}]) > 10.3$) at $z \sim 0.7\text{--}3.7$ within the KMOS^{3D} survey. We spatially resolve 23 compact SFGs and find that the majority are dominated by rotational motions with velocities ranging from 95 to 500 km s⁻¹. The range of rotation velocities is reflected in a similar range of integrated H α line widths, 75–400 km s⁻¹, consistent with the kinematic properties of mass-matched extended galaxies from the full KMOS^{3D} sample. The fraction of compact SFGs that are classified as “rotation-dominated” or “disklike” also mirrors the fractions of the full KMOS^{3D} sample. We show that integrated line-of-sight gas velocity dispersions from KMOS^{3D} are best approximated by a linear combination of their rotation and turbulent velocities with a lesser but still significant contribution from galactic-scale winds. The H α exponential disk sizes of compact SFGs are, on average, 2.5 ± 0.2 kpc, $1\text{--}2\times$ the continuum sizes, in agreement with previous work. The compact SFGs have a $1.4\times$ higher active galactic nucleus (AGN) incidence than the full KMOS^{3D} sample at fixed stellar mass with an average AGN fraction of 76%. Given their high and centrally concentrated stellar masses, as well as stellar-to-dynamical mass ratios close to unity, the compact SFGs are likely to have low molecular gas fractions and to quench on a short timescale unless replenished with inflowing gas. The rotation in these compact systems suggests that their direct descendants are rotating passive galaxies.

Key words: galaxies: evolution – galaxies: high-redshift – galaxies: kinematics and dynamics – infrared: galaxies

1. Introduction

The transformation of a star-forming galaxy (SFG) into a passive galaxy is a key process in galaxy evolution. Yet the details of how SFGs are quenched are mostly unknown, particularly in the early universe. Studies of the high-redshift galaxy population have shown that quiescent galaxies at $z \gtrsim 1$ are much more compact than their local counterparts (e.g., Trujillo et al. 2007; van Dokkum et al. 2008; Damjanov et al. 2009; Newman et al. 2012). Their small sizes suggest that they were either created from larger SFGs through highly dissipative processes or formed from already compact SFGs. These different formation histories imply different quenching mechanisms.

There are many well-supported candidates for quenching—e.g., environment and mass—and evidence that different mechanisms act in tandem (e.g., Toomre & Toomre 1972; Mihos & Hernquist

1994; Hopkins et al. 2010; Peng et al. 2010; Fossati et al. 2017). However, because the transition of individual galaxies from star-forming to passive can be rapid (Balogh et al. 2004; Martin et al. 2007), it is particularly difficult to observe individual cases. Instead, progress in understanding the cessation of star formation typically comes from studies of statistical samples where comparisons can be drawn between the global properties of star-forming and passive galaxy populations. Global properties, e.g., color, structural properties, size-mass, star formation rate-mass, often show a bimodality with a small number of galaxies creating a bridge between the star-forming and passive populations. The galaxies in between may represent an interesting class of galaxies currently undergoing a transformation.

In recent years, observational studies have shown that the quenching of star formation is intimately linked to the formation of a bulge (e.g., Bluck et al. 2014; Lang et al. 2014), lending support to an association between early-type morphology and quiescence. Galaxies in transition are expected to change their morphologies prior to quenching, stimulated, for example, by interactions with other galaxies or their environments (e.g., Toomre & Toomre 1972; Mihos & Hernquist 1994; Naab &

* Based on observations obtained at the Very Large Telescope (VLT) of the European Southern Observatory (ESO), Paranal, Chile (ESO program IDs 092A-0091, 093.A-0079, 094.A-0217, 095.A-0047, 096.A-0025, 097.A-0028, and 098.A-0045).

Burkert 2003). Major mergers can drive the formation of spheroids either directly or by triggering massive central starbursts (Hopkins et al. 2010); however, internal disk instabilities, either secular or merger-induced, are also expected to drive efficient radial inflows that can lead to a buildup of central stellar mass density (Bournaud et al. 2007; Dekel & Burkert 2014; Brennan et al. 2015).

The same mechanisms are expected as possible pathways from star-forming to quiescence in the early universe. In high-redshift disks, violent internal instabilities and gas-rich mergers could lead to dissipative processes able to form a massive, compact bulge that can either exhaust the available gas or stabilize it against further collapse (Martig et al. 2009; Dekel & Burkert 2014; Genzel et al. 2014a; Zolotov et al. 2015). In such a scenario, star formation is expected to wind down on \sim Gyr timescales, resulting in young, quenched spheroids (Barro et al. 2014a; Dekel & Burkert 2014).

Some models have shown that prior to being quenched, galaxies exist in a compact-core or dense phase for a short time while still hosting significant star formation (Dekel & Burkert 2014; Wellons et al. 2015; Tacchella et al. 2016). These galaxies, while rare, have been increasingly identified in large data sets that have become available from both observations (e.g., CANDELS; Grogin et al. 2011; Koekemoer et al. 2011) and simulations (e.g., EAGLE: Schaye et al. 2015; Crain et al. 2015; ILLUSTRIS: Vogelsberger et al. 2014; Genel et al. 2014). Thus, these “compact star-forming galaxies” (SFGs) are possible immediate progenitors to distant compact quiescent galaxies. Observationally, they are dense and compact (<3 kpc; Barro et al. 2013, 2014a; Nelson et al. 2014), dusty (van Dokkum et al. 2015), and, despite often being branded as “blue nuggets,” red in color (Barro et al. 2013). While such characteristics are in line with expectations from “wet compaction,” there is also observational support for the scenario in which compact SFGs grow inside-out from already compact higher-redshift progenitors (van Dokkum et al. 2015; Wellons et al. 2015).

While the sizes, colors, and star formation rates (SFRs) of these possible progenitors are well characterized, the dynamics of these systems are still being pieced together. Due to their small sizes, obtaining resolved dynamical information has been difficult (Barro et al. 2014b; Nelson et al. 2014; van Dokkum et al. 2015). Given their high central masses, it is predicted that these objects will also have high central velocity dispersions in both gas and stars (Bell et al. 2012; Wake et al. 2012; Fang et al. 2013; Bezanson et al. 2015; van Dokkum et al. 2015; Beifiori et al. 2017), further linking them to quiescent galaxies at similar redshifts (van de Sande et al. 2013; Belli et al. 2014). Indeed, the first spectral measurements of compact SFGs at $z \sim 2$ have revealed large integrated gas velocity dispersions, ~ 200 km s $^{-1}$ (Barro et al. 2014b; Nelson et al. 2014), comparable to stellar velocity dispersions of massive quiescent galaxies at similar redshifts. However, to what extent rotation, dispersion, and galactic winds contribute to the integrated line widths is unknown, thus making use of the integrated line width as a dynamical mass indicator highly uncertain.

The past 15 yr have revealed that massive quiescent galaxies in the local universe feature a mixture of kinematic signatures defined by both rotation and pressure support (e.g., Emsellem et al. 2007, 2011; Cappellari et al. 2011). Given these results and the prevalence of massive high-redshift disk galaxies with prominent bulges (e.g., Lang et al. 2014), it is highly likely that

at least a fraction of high-redshift quiescent galaxies and their progenitors also show disklike morphologies and/or axial ratio distributions. Imaging studies lend credence to this hypothesis, with 65% of compact quiescent galaxies showing disklike morphologies (van der Wel et al. 2011; Chang et al. 2013). Furthermore, stellar rotation >100 km s $^{-1}$ has now been measured directly in two fortuitously strongly lensed $z > 2$ quiescent galaxies (Newman et al. 2015; Toft et al. 2017). Recent long- and multislit results of possible progenitors to compact quiescent galaxies have also shown evidence for rotation-dominated kinematics (van Dokkum et al. 2015).

An additional factor that may contribute to the shutdown of star formation in these systems is the role of active galactic nuclei (AGNs) and AGN feedback (Bower et al. 2006; Croton et al. 2006). Compact SFGs are preferentially massive; thus, high AGN fractions are expected (e.g., Kauffmann et al. 2003a; Reddy et al. 2005; Brusa et al. 2009). This is reflected in modern simulations where the black hole accretion rate is tied to the density of the surrounding gas (Wellons et al. 2015). The observational signatures of AGNs and AGN-driven outflows are commonly seen in the kinematics of high-redshift galaxies and increasingly prevalent at the massive end of the star-forming “main sequence” (MS; e.g., Shapiro et al. 2009; Alexander et al. 2010; Förster Schreiber et al. 2014; Genzel et al. 2014b; N. M. Förster Schreiber et al. 2018, in preparation).

Here we exploit the 3D information and depth of our KMOS^{3D} survey (Wisnioski et al. 2015; hereafter **W15**) to take the next step in addressing the kinematic nature of compact SFGs, set quantitative constraints on the processes driving their emission-line widths, and shed new light on the connection to compact quiescent galaxies at similar redshifts.

We present the first integral field spectroscopic observations of 35 compact dense-core SFGs. In Section 2, we discuss the selection techniques of compact and dense galaxies. In Section 3, we present our resolved KMOS^{3D} results and investigate kinematic tracers of the potential using the rotational velocity and integrated line widths. In Section 4, we discuss the implications of our results on the possible evolutionary pathways for both creating and evolving compact SFGs. We conclude with our results in Section 5. We assume a Λ CDM cosmology with $H_0 = 70$ km s $^{-1}$ Mpc $^{-1}$, $\Omega_m = 0.3$, and $\Omega_\Lambda = 0.7$. For this cosmology, 1'' corresponds to ~ 7.8 kpc at $z = 0.9$, ~ 8.2 kpc at $z = 2.3$, and ~ 7.2 kpc at $z = 3.6$. We adopt a Chabrier (2003) initial mass function.

2. Data

2.1. KMOS Observations and Data Analysis

KMOS^{3D} is an ongoing kinematic survey using the K-band Multi-Object Spectrograph (KMOS; Sharples et al. 2013) to obtain near-infrared (IR) integral field spectroscopy covering the [N II]+H α emission-line complex at $0.7 < z < 2.7$. Targets were selected from the 3D-*HST* Legacy Survey (Brammer et al. 2012; Skelton et al. 2014; Momcheva et al. 2016) and CANDELS (Grogin et al. 2011; Koekemoer et al. 2011) in COSMOS, GOODS-S, and UDS, and the primary sample includes galaxies with $K_s \leq 23$ and a prior redshift (3D-*HST*) that places H α in a region of the spectrum relatively free of contamination from OH sky lines. In addition, we also include data covering [O III]+H β for narrow-band selected galaxies extending up to $z = 3.7$ also observed in KMOS^{3D} pointings.

The KMOS^{3D} sample includes galaxies spanning more than 4 orders of magnitude in specific star formation rate (sSFR) because the target selection does not include any a priori information on SFR. In this work, we identify SFGs based on their positions relative to the MS such that $\Delta\text{SFR} \equiv \log(\text{SFR}_{\text{UV+IR}}/\text{SFR}_{\text{MS}}) > -0.85$, where SFR_{MS} is defined by the 3D-*HST* MS (Whitaker et al. 2014) for each galaxy given its redshift and stellar mass using the parameterization of W15. The SFRs are derived by combining the unobscured (UV) and obscured (IR) star formation following Wuyts et al. (2011a) or from the spectral energy distribution (SED) if there is no IR detection. We note that the adopted cut between star-forming and passive galaxies for this paper is similar to an evolving *UVJ* selection; however, for the purposes of investigating possible progenitors of quenched galaxies, we do not want to rule out galaxies with *UVJ* passive colors that have residual star formation (Barro et al. 2013; Belli et al. 2017a).

Full details of the KMOS^{3D} observing conditions, observing strategy, and data reduction procedure are given in W15 and a forthcoming data release paper. Relevant details for this work are described briefly in the following paragraphs.

Observations of KMOS^{3D} data used here were carried out between 2013 October and 2017 September with exposure times ranging from 3 to 30 hr on source. Data were collected in excellent seeing conditions, *YJ*-, *H*-, or *K*-band median seeing FWHM = 0".55. The model-independent seeing is measured as the FWHM from stars observed simultaneously in the same waveband and detector as the galaxy observations. For the compact sources discussed in greater detail in this paper, the median seeing was 0".5 with individual values ranging from 0.42 to 0.61.

We map the kinematics across the emission-line-detected regions of the galaxy using single Gaussian fits after applying a 3×3 pixel spatial median filter. The median filtering is used only to create the kinematic map. Integrated spectra and 1D kinematic extractions are extracted directly from the original data cube. The kinematic axis is determined from the 2D velocity field as the direction of the largest observed velocity difference. One-dimensional kinematic profiles are extracted along the kinematic major axis using an aperture equivalent to the point spread function (PSF), unique to each galaxy. When a kinematic axis cannot be determined from the 2D velocity field, the photometric major axis is used for the 1D extractions. Galaxies are considered resolved when emission lines can be fit to a radius of $1.5 \times$ the PSF FWHM from the center of the continuum emission. The 1D kinematic profiles allow measurements slightly beyond the extent of individual spaxels, as they are measured from summed spectra within an aperture. In resolved cases, we derive an estimate of the observed velocity difference along the kinematic major axis, v_{obs} ; rotational velocity, $v_{\text{rot}} = v_{\text{obs}}/\sin i$; and disk velocity dispersion, σ_0 . We estimate $\sin i$ using the *HST H*-band (F160W) structural axis ratio (b/a) assuming a thick disk with a ratio of scale height to scale length of 0.25. Structural parameters are drawn from Lang et al. (2014) based on single-component GALFIT (Peng et al. 2002) models (see also van der Wel et al. 2014). We derive integrated spectra for all KMOS^{3D} galaxies by summing over spaxels within a 1".5 diameter aperture. The velocity gradients are not removed from these spectra. Good spaxel masks are created for resolved galaxies. They include spaxels where the signal-to-noise ratio (S/N) of H α or [O III] is >5 ,

velocity uncertainties are $<100 \text{ km s}^{-1}$, and/or a relative velocity dispersion uncertainty is $<50\%$.

The KMOS observations are seeing-limited and subject to beam smearing. Beam-smearing corrections used to calculate the corrected rotational velocity, $v_{\text{rot,corr}}$, and disk velocity dispersion, $\sigma_{0,\text{corr}}$, are derived following the methods in Appendix A.2.4 of Burkert et al. (2016). In short, multiplicative beam-smearing corrections are derived from a set of exponential disk dynamical models run at different inclinations, masses, ratios of half-light size to PSF size, velocity dispersions, and instrumental resolutions. To determine a beam-smearing correction for an individual galaxy, a relation relating the ratios of half-light size/PSF size to the magnitude of the beam-smearing correction is queried based on the properties of the specific galaxy and observed PSF. The typical magnitude of the beam-smearing corrections for the compact sources discussed here is discussed at the end of Section 3.3. For a more detailed description of the methods used to derive the kinematic maps and subsequent parameters, we refer the reader to W15 and Appendix A of Burkert et al. (2016).

2.2. Compact Galaxy Selection

Our selection of compact galaxies relies primarily on two parameters: the global compactness $\Sigma_{1.5} (\equiv M_*/r_e^{1.5})$, where r_e is the *HST H* band (F160W) circularized half-light size (Barro et al. 2013), and the stellar surface density within the central 1 kpc, $\Sigma_{1\text{kpc}}$. We compute $\Sigma_{1\text{kpc}}$ by integrating over the deprojected luminosity density distribution as described by van Dokkum et al. (2014). We additionally require that compact galaxies are massive, $M_* > 10^{10} M_\odot$. Figure 1 shows the distribution of KMOS^{3D} galaxies in terms of their SFR, compactness (top panels), and central density (bottom panels) in three redshift ranges corresponding to the KMOS *YJ*, *H*, and *K* bands.

While selecting on global compactness identifies galaxies morphologically similar to compact quiescent galaxies (axis ratios of approximately unity and small sizes; $r_e < 2$ kpc), selecting on central density identifies galaxies with a variety of sizes and axial ratios but with the presence of a dense stellar core, often seen as a requirement for quenching (e.g., Cheung et al. 2012; Bluck et al. 2014; Lang et al. 2014; van Dokkum et al. 2014). In Figure 1, the blue circles show the SFGs selected on global compactness using $\log(\Sigma_{1.5}) > 10.3$ (Barro et al. 2013). Their location in the bottom panels shows the overlap of what would be selected as compact rather than as containing a dense core using $\log(\Sigma_{1\text{kpc}}) > 9.5$. Galaxies observed in KMOS^{3D} are identified by in the top panels. Figure 2 shows examples of the types of galaxies selected by these two different criteria separately. While the galaxies in the top panels are compact, they do not closely resemble quiescent galaxies at $z \approx 1-3$, which is a key motivation to study the compact SFGs. In contrast, the bottom panels show galaxies with bulge components reminiscent of quiescent galaxies surrounded by large blue disks. We adopt as our final “compact” sample those galaxies satisfying both the global compactness and central density criteria ($\log(\Sigma_{1.5}) > 10.3$ and $\log(\Sigma_{1\text{kpc}}) > 9.5$).

Of the 502 “star-forming” galaxies, $\Delta\text{SFR} > -0.85$, in our KMOS^{3D} sample (as of 2016 December), 45 satisfy both the compactness and central density criteria, and 35 of these are detected, spanning the redshift range $0.9 < z < 3.7$, including both H α (33) and [O III] (2) detected galaxies. The composite *HST IJH* images, integrated spectra, and exposure times for these

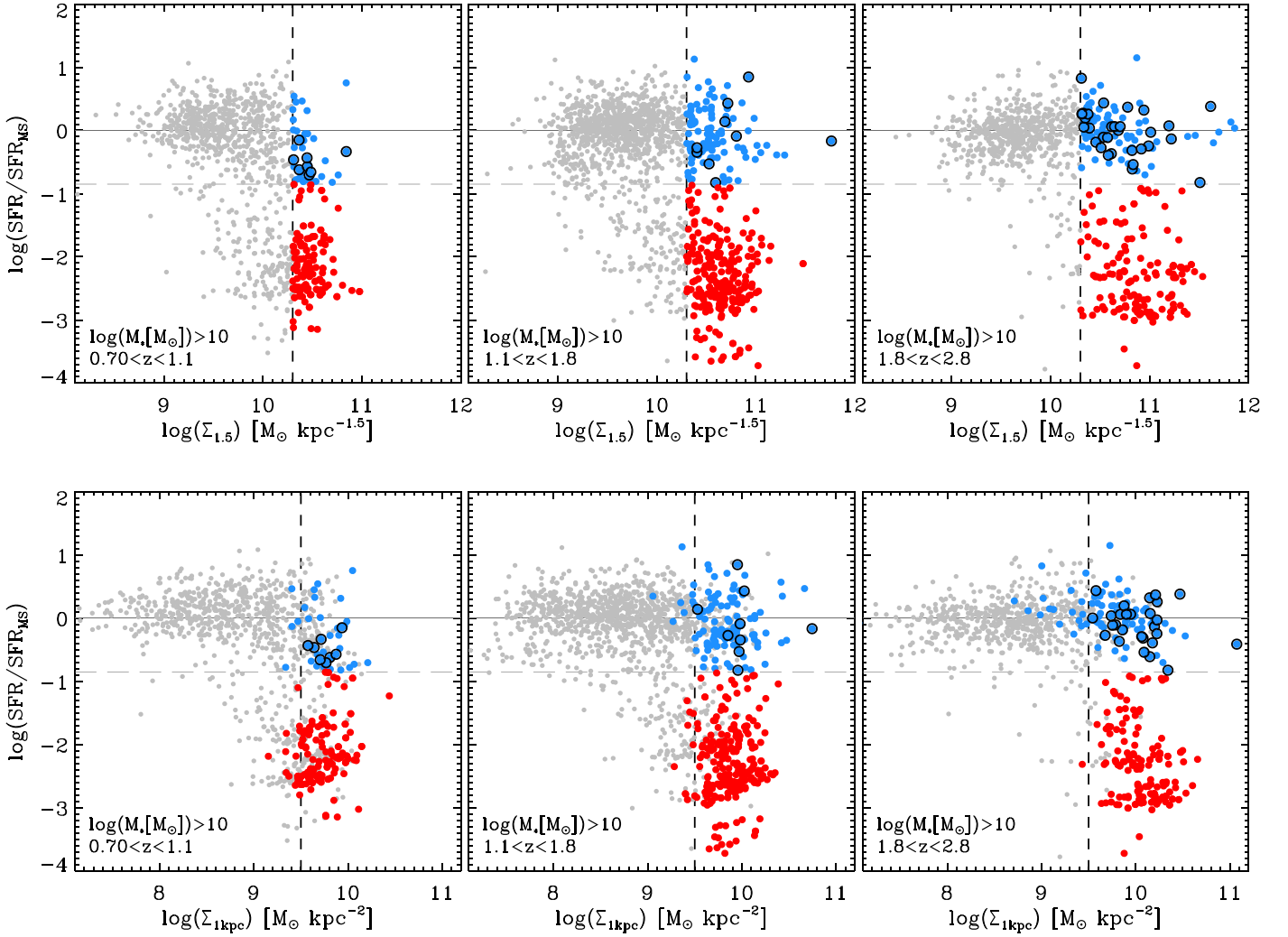


Figure 1. SFR/SFR_{MS} vs. compactness, $\Sigma_{1.5}$ (top panels), and inner kpc density, $\Sigma_{1\text{kpc}}$ (bottom panels), as measured from *HST* *H*-band half-light sizes for galaxies in v4.1.5 3D-*HST*/CANDELS satisfying the KMOS^{3D} magnitude and visibility selection criteria. The three columns show the selection diagram in three redshift bins, $0.7 < z < 1.1$, $1.1 < z < 1.8$, and $1.8 < z < 2.8$. The horizontal solid lines denote the canonical MS as defined by the 3D-*HST* MS (Whitaker et al. 2014). Blue circles are SFGs ($\Delta\text{SFR} > -0.85$; horizontal dashed lines) with $\log(\Sigma_{1.5}) > 10.3$ (vertical dashed lines), and red circles are quiescent galaxies ($\Delta\text{SFR} < -0.85$) with $\log(\Sigma_{1.5}) > 10.3$. Black circles highlight galaxies observed in KMOS^{3D} that have been selected as compact SFGs following the criteria $\log(\Sigma_{1.5}) > 10.3$, $\log(\Sigma_{1\text{kpc}}) > 9.5$, $\Delta\text{SFR} > -0.85$, and $M_* > 10^{10} M_\odot$.

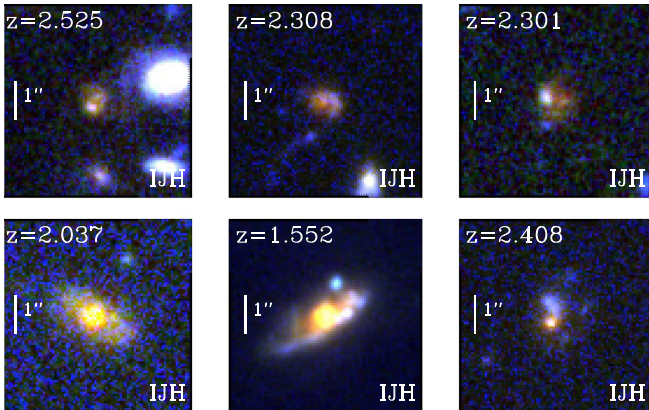


Figure 2. Example composite *HST* IJH images showing galaxies exclusively satisfying the selection of either compact galaxies ($\log(\Sigma_{1.5}[M_\odot \text{kpc}^{-1.5}]) > 10.3$; top) or dense-core galaxies ($\log(\Sigma_{1\text{kpc}}[M_\odot \text{kpc}^{-2}]) > 9.5$; bottom).

objects are shown in Figure 3, ordered by increasing redshift. Integrated spectra for each galaxy are created by summing the spaxels in a $1''.5$ diameter aperture. Single-component Gaussian fits are overplotted in red.

The average half-light radius, Sérsic index, axis ratio, and bulge-to-total (B/T) of the detected compact SFGs are 1.85 kpc, 3.9, 0.72, and 0.5, respectively, compared to 1.36 kpc, 3.7, 0.65, and 0.7 for compact quiescent galaxies selected using the same criteria. However, we note that some of these galaxies are close to the resolution limit of *HST* in the *H* band, resulting in large uncertainties in structural parameters not included in the formal errors. For example, of the 35 detected galaxies, six have unconstrained Sérsic indices of either 0.2 or 8.0, the limits of the fitting range. We note that three of the six are Type I AGNs, as discussed in the next section.

Ten of the detected compact SFGs have rest-frame colors consistent with being passive using a *UVJ* color selection (e.g.,

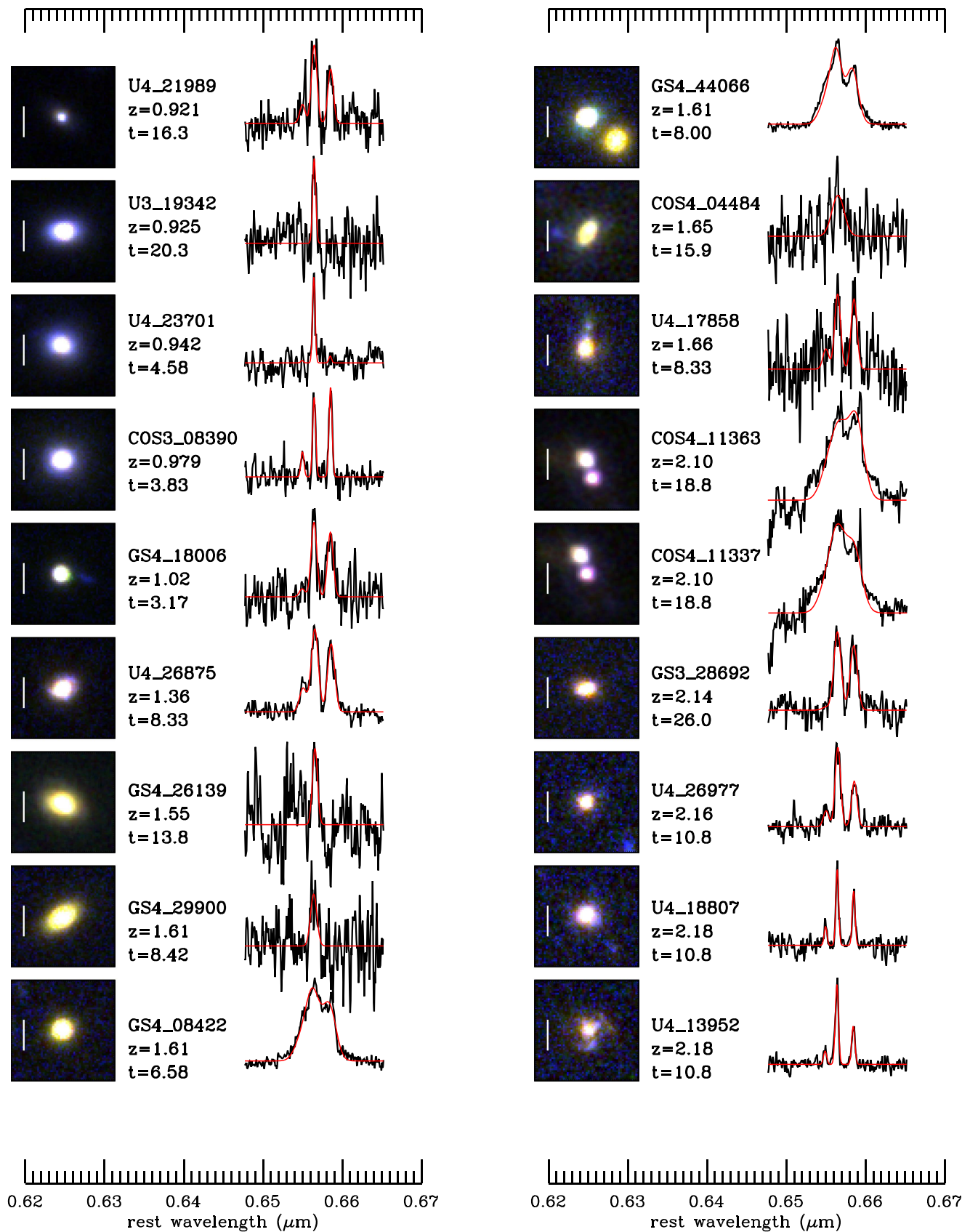


Figure 3. *HST* observed-frame *IJH* images and *KMOS*^{3D} integrated spectra of $H\alpha$ -[N II] or $H\beta$ -[O III] emission complexes for the detected galaxies that are both centrally dense and compact as defined by $\log(\Sigma_{1.5}) > 10.3$ and $\log(\Sigma_{1\text{kpc}}) > 9.5$. The spectra are σ -clipped and normalized to arbitrary flux units. Single Gaussian fits to the $H\alpha$ -[N II] or $H\beta$ -[O III] complex are overlaid in red. Observation times, t , are given in hours for each object. White bars in the images show $1''$. Galaxies are shown in order of increasing redshift. We note that the spectra of COS4_11363 and COS4_11337 are blended in the *KMOS*^{3D} data due to their small separation on the sky.

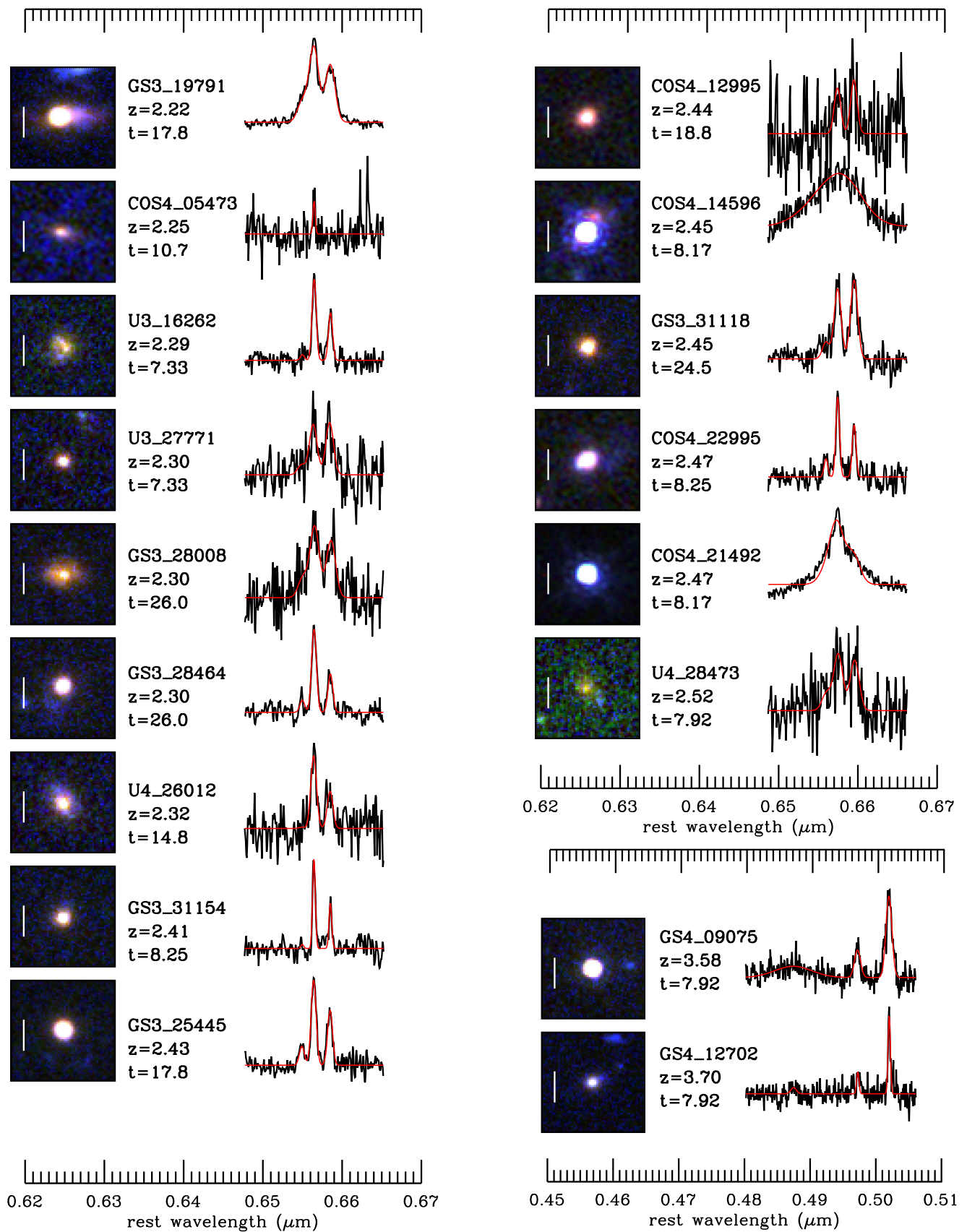


Figure 3. (Continued.)

Muzzin et al. 2013). In addition to the compact SFG sample, we robustly detect $H\alpha$ in 15 compact quiescent galaxies ($\Delta SFR < -0.85$), of which two are resolved. The properties of $H\alpha$ -detected quiescent galaxies are discussed in Belli et al. (2017a).

We find that 76% of the detected compact SFGs may host an AGN. In the general SFG population, AGN incidence is a strong function of stellar mass (e.g., Kauffmann et al. 2003a). In addition to optical indicators, this has also been shown using UV, IR, and X-ray indicators (e.g., Best et al. 2005; Bundy et al. 2008). Combining X-ray, IR, and radio data confirms that the high-mass galaxies, in particular the compact dense galaxies in KMOS^{3D}, have high AGN fractions, as also shown by Barro et al. (2013) and Kocevski et al. (2017). Using techniques described in Genzel et al. (2014b) to identify likely AGN hosts, we recover this trend in our full observed sample.

In concordance, nuclear activity is prevalent in the KMOS^{3D} high-mass galaxies as determined from high $[N II]/H\alpha$ ratios ($\log([N II]/H\alpha) > -0.1$) and the presence of an underlying broad $H\alpha$ emission component (Genzel et al. 2014b; N. M. Förster Schreiber et al. 2018, in preparation). These results are consistent with the rapid increase of outflow incidence as a function of stellar mass, as shown in our previous studies (Förster Schreiber et al. 2014; Genzel et al. 2014b) and updated with an approximately $5\times$ larger sample (N. M. Förster Schreiber et al. 2018, in preparation), as well as with general trends with increasing central stellar mass density. We find that 45% of all observed KMOS^{3D} SFGs exhibit high $[N II]/H\alpha$ or a broad component in the stellar mass range $10.5 < \log(M_*/M_\odot) < 11.7$. Dense compact galaxies are among the most massive KMOS^{3D} galaxies by selection and show $\sim 1.2\times$ higher fractions of spectral signatures of nuclear activity than the full population, with 55% in the same mass range. When taking into account all five AGN indicators from Genzel et al. (2014b) for the full KMOS^{3D} sample in the stellar mass range $10.5 < \log(M_*/M_\odot) < 11.7$, the AGN fraction is 53%, compared to 76% for dense compact SFGs.

Fitting a single Gaussian to the spectrum of a galaxy hosting a outflow can result in an artificially larger line width, with the strongest effect most likely to occur for shallow data strongly light-weighted by bright central regions where the presence of a centrally driven wind can dominate (Förster Schreiber et al. 2014; Genzel et al. 2014b). This effect is investigated further in Section 3.4.

Three compact SFGs are possible Type I AGNs, as indicated from the combination of KMOS spectra, X-rays, and rest UV data, two of which have $\sigma_{\text{tot}} > 500 \text{ km s}^{-1}$ from a single Gaussian fit to the KMOS data. The *HST* images of these three galaxies, COS4_14596, COS4_21492, and GS4_09075, exhibit characteristics of the PSF, such as diffraction spikes and spots. We exclude these objects from our further analysis of the integrated line-width and emission-line ratios.

3. Results

3.1. $H\alpha$ Sizes

We measured intrinsic $H\alpha$ or $[O III]$ sizes for galaxies in our compact SFG sample by fitting a pure exponential disk profile convolved with the KMOS PSF to 2D KMOS emission maps with the centroid, ellipticity, and position angle (PA) fixed to that of the continuum map in the *HST* F160W band (Erwin 2015). The flux in individual spaxels was estimated by

integrating the continuum-subtracted spectrum within a $\pm 200 \text{ km s}^{-1}$ window centered on the expected wavelength of the emission line, derived either from a single-component Gaussian fit to the line or, in the case of low-S/N regions, the nearest spaxel with a successful fit. In this way, we were able to derive emission maps extending over the full KMOS field of view. For each galaxy, we construct a model of the KMOS PSF by stacking registered images of individual PSF stars taken in the same exposure and detector. We note that, due to uncertainties in the relative position of the KMOS arms (~ 0.2 rms), this procedure likely underestimates the “true” PSF FWHM; however, we do not expect it to significantly affect our conclusions. Uncertainties on the sizes were estimated from bootstrap realizations of the combined KMOS data, where individual 300 s exposures were randomly recombined with replacement. Further details of the modeling procedure will be described in a future paper (D. Wilman et al. 2018, in preparation).

The average intrinsic $H\alpha$ half-light size of the compact SFGs is 2.5 ± 0.2 kpc. The $H\alpha$ sizes are typically between $1\times$ and $2\times$ the continuum sizes as measured from single Sérsic fits to the CANDELS F160W images, with 33% agreeing with a size ratio of unity within 1σ errors. The average size ratio, $r_{H\alpha}/r_e[\text{F160W}]$, is 1.2 but ranges between 0.7 and 4.1. The size ratios are consistent with the size ratios found for the most massive galaxies in the 3D-*HST* survey at $z \sim 1$ (Nelson et al. 2016), and the $H\alpha$ sizes of the KMOS^{3D} compact SFGs are comparable to those derived from position–velocity diagrams of long- and multislit observations of compact SFGs (van Dokkum et al. 2015).

The $H\alpha$ sizes also show good agreement with the rest-frame *UV* emission as probed by the observed *I*-band distribution at these redshifts. Some compact SFGs in our sample do exhibit faint emission in the *I* and *J* bands as seen in the composite *IJH* images of Figure 3 with either asymmetric emission around the dominant *H*-band light (e.g., U4_17858 and COS4_22995) or extended emission reminiscent of a faint disk or spiral features (e.g., GS3_19791 and U4_26012). The galaxies with visible features in the *I* band are among the galaxies with the largest $H\alpha$ sizes. In contrast, some simulations predict faint outer disks or rings surrounding compact SFGs (Zolotov et al. 2015). Galaxies in the KMOS^{3D} sample that do fit the description of centrally dense cores surrounded by large (>2 kpc) star-forming rings are the extended centrally dense galaxies shown in the bottom panels of Figure 2.

3.2. Compact SFG Unresolved Kinematics

For all detected compact SFGs, we measure an integrated line width, σ_{tot} , from single Gaussian fits to the $H\alpha$ - $[N II]$ or $[O III]$ complex of the non-velocity-shifted integrated spectrum and correct for spectral resolution. The line widths of compact SFGs cover a wide range, $75\text{--}400 \text{ km s}^{-1}$. In Figure 4, we show the relationship between $H\alpha$ velocity dispersion and stellar mass for extended and compact SFGs from KMOS^{3D}. Compact SFGs from the literature are shown by green diamonds (Barro et al. 2014b; van Dokkum et al. 2015). We also compare our results to a complementary quiescent galaxy field survey with KMOS, the VLT IR IFU Absorption Line survey (VIRIAL; Mendel et al. 2015; J. T. Mendel 2018, in preparation). VIRIAL targets are *UVJ* passive galaxies selected from the 3D-*HST* survey. The velocity dispersions for the

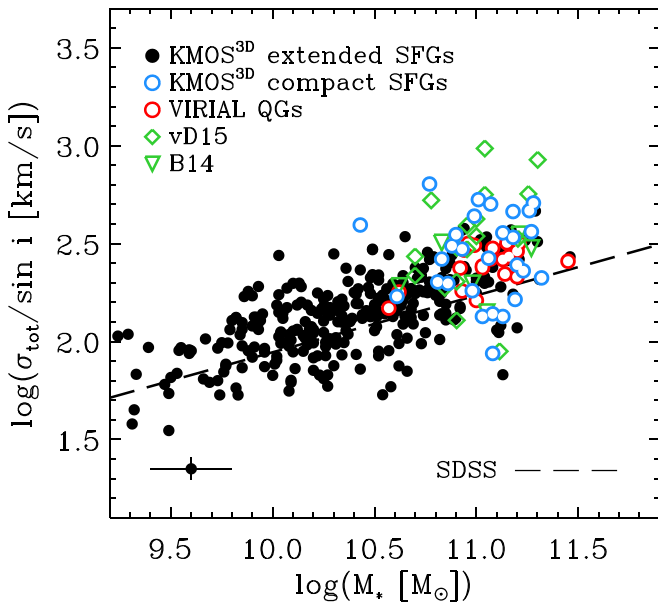


Figure 4. Inclination-corrected integrated line width vs. M_* . The dashed line shows the relation derived from SDSS (Fang et al. 2013). All SFGs from KMOS^{3D} are shown by black and blue circles, literature compact SFGs (Barro et al. 2014b; van Dokkum et al. 2015) are shown by green diamonds, and quiescent galaxies from VIRIAL are shown by red circles. For SFGs, σ_{tot} is measured from H α or [O III] emission. In the case of galaxies observed in KMOS^{3D} and the literature, only the KMOS^{3D} galaxies are shown. For quiescent galaxies, σ_{tot} is measured from stellar absorption features (J. T. Mendel et al. 2018, in preparation). All SFGs, with the exception of values from Barro et al. (2014b), are corrected for inclination. A representative error bar is shown in the bottom left corner.

VIRIAL survey are measured from the absorption lines of unresolved compact galaxies. Under the assumption that the majority of our sample is rotating, we apply a simple $\sin i$ correction to all KMOS^{3D} galaxies to account for inclination effects (in W15, we show that 83% of SFGs at these epochs are rotationally supported). In contrast, we do not apply a $\sin i$ correction to the passive galaxy sample, which we restrict to systems with $n > 2$ (Belli et al. 2017b).

Figure 4 shows that the compact SFGs form the high-mass end of the trend established from the general SFG population. The line widths of compact SFGs are consistent with the line widths of extended SFGs from the KMOS^{3D} survey of similar mass and redshift. Compact SFGs from the literature overlap but, on average, have slightly larger line widths for their mass than when compared to the KMOS^{3D} data. This may be a result of selection, shallower data, or contamination by nuclear-driven outflows. In general, the H α velocity dispersions of compact SFGs show excellent agreement with the central stellar velocity dispersion of quiescent galaxies at equivalent redshifts and masses. We note that there are some ambiguities in comparing stellar and gas velocity dispersions; however, because σ_{tot} encompasses both rotation and turbulence, it should trace the total dynamical mass of the galaxy comparable to central stellar dispersions (e.g., Weiner et al. 2006; Kassin et al. 2007; Cappellari et al. 2013; Courteau et al. 2014; Guerou et al. 2017). We investigate the relationship between σ_{tot} and rotational and dispersion velocities in Section 3.4.

Locally, a tight relationship between central velocity dispersion and stellar mass has been established for both quiescent galaxies and SFGs (Wake et al. 2012; Fang et al. 2013). We recover a correlation over two orders of magnitude between σ_{tot} and M_* with a consistent slope and

factor of ~ 1.38 offset from the local relation parameterized by Fang et al. (2013) with SDSS.¹³ The slight offset of the population from the local relation could be explained by evolutionary effects. For example, it is well known that for SFGs, the integrated line width is correlated with rotational velocity, both locally and at high redshift (e.g., Tully & Fouque 1985; Weiner et al. 2006). Thus, Figure 4 roughly presents a stellar Tully–Fisher relation (Tully & Fisher 1977; Übler et al. 2017). The details of the relationship between σ_{tot} and velocity are less clear and may also change with redshift. This is explored in greater detail for the full KMOS^{3D} sample in Section 3.4.

3.3. Compact SFG Resolved Kinematics

We resolve line emission in 23 of the 35 compact SFGs detected in KMOS^{3D}, spanning the wide redshift range of $0.9 < z < 3.7$. The fraction of resolved compact SFGs, $\sim 66\%$, is marginally lower than the resolved fraction in the full KMOS^{3D} sample of 74%. In Section 4.1 of W15, we outline in detail a set of five criteria used for the KMOS^{3D} survey to classify galaxies as “rotation-dominated” and “disklike.” The criteria are (1) a clear monotonic velocity gradient; (2) the ratio of rotational support to the disk velocity dispersion measured in the outer parts of the galaxy, v_{rot}/σ_0 , being greater than unity; (3) the agreement of the photometric and kinematic axes within 30° ; (4) the spatial coincidence of the centroids of the velocity map and velocity dispersion map within the errors; and (5) the spatial coincidence of the centroids of the velocity map and the continuum map within the errors. Of the KMOS^{3D} compact SFGs that are resolved, 21/23 satisfy the first two criteria to be considered rotation-dominated, and 12/23 satisfy the more strict five criteria to be considered disklike. These fractions are consistent with the same analysis for the full KMOS^{3D} galaxy sample of 83% and 58%, respectively, as reported in W15. In Figure 5, we show the 1D and 2D kinematics of the compact SFGs that are rotation-dominated.

Rotationally supported compact SFGs have mean inclination and beam-smearing-corrected velocities of 267 km s^{-1} and mean $v_{\text{rot,corr}}/\sigma_{0,\text{corr}} = 4.6$, comparable to extended disklike SFGs from the full KMOS^{3D} sample. We discuss these properties in the context of the overall sample in Section 3.4. Typical uncertainties on $v_{\text{rot,corr}}$ and $\sigma_{0,\text{corr}}$ are 25% and 30%, respectively. The main uncertainties for kinematic measurement of these compact galaxies are discussed further at the end of this section. Disk circular velocities are estimated for the galaxies satisfying all five disk criteria by correcting for the effects of inclination, beam smearing, and additional pressure support from random motions, such that

$$v_d = \sqrt{v_{\text{rot,corr}}^2 + \alpha \sigma_{0,\text{corr}}^2}. \quad (1)$$

The functional form of α is dependent on the distribution of gas surface density and gas velocity dispersion (Valenzuela

¹³ The local relation is established using fiber-based central stellar velocity dispersions corrected to a radius of 1 kpc using Equation (1) of Cappellari et al. (2006). We do not know if the intrinsic dispersion curves mirror those in Cappellari et al. (2006), and observational evidence indicates that they may be flat (Cresci et al. 2009), resulting in a null correction. However, if we assume that the dispersion curves have comparable radial profiles to the galaxies in Cappellari et al. (2006) and apply the same correction, then the KMOS^{3D} line widths would increase by ~ 1.09 , with the highest factors being 1.15 for the few galaxies with half-light radii > 8 kpc and the smallest correction factors being for compact SFGs and quiescent galaxies.

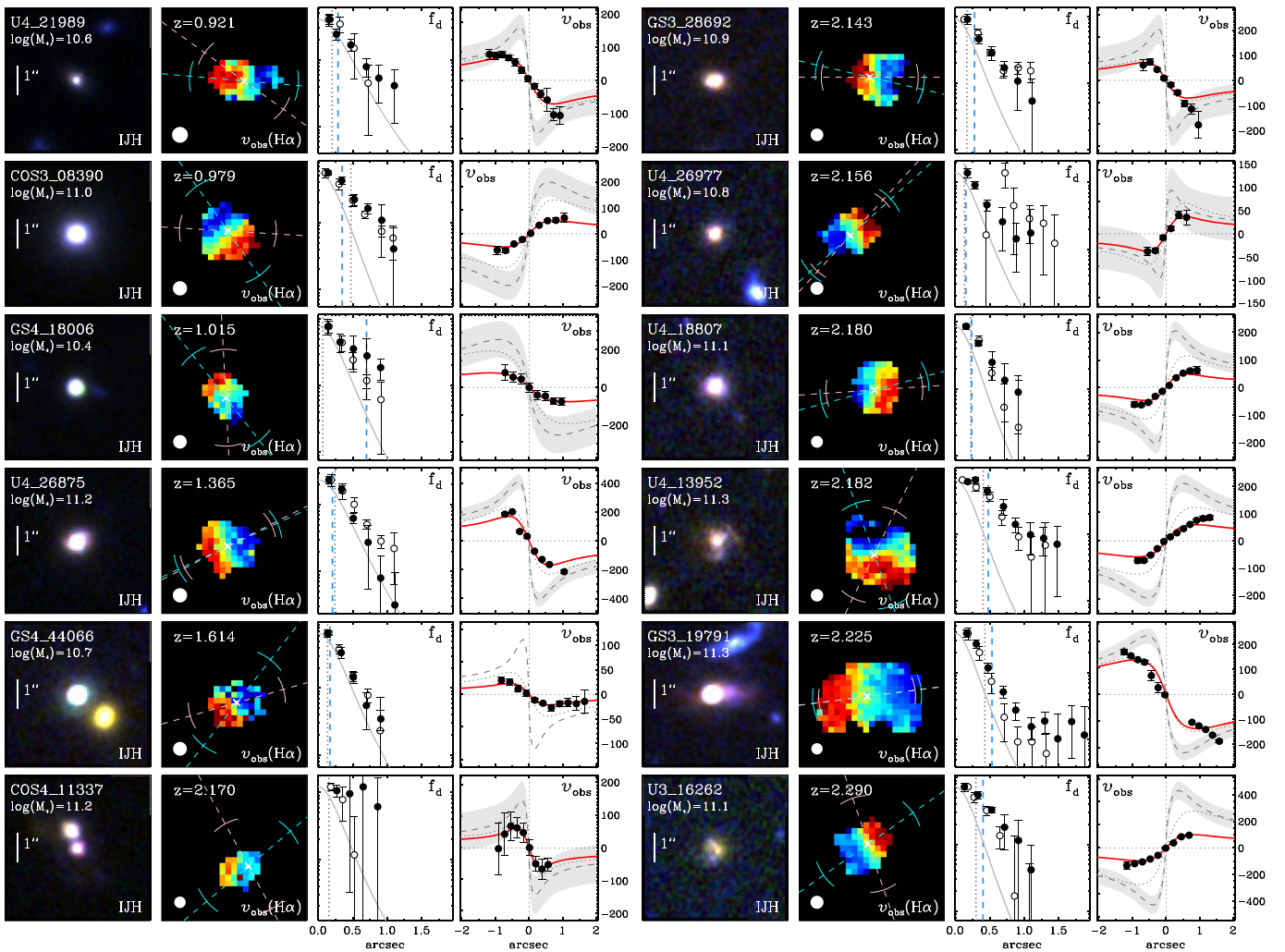


Figure 5. (Left) Extracted 2D and 1D kinematics of all rotationally dominated compact SFGs in our sample. From left to right: *HST* IJH color composite image; KMOS^{3D} H α velocity map, shown with a FWHM of the PSF specific to observations of this galaxy (white circle); normalized KMOS continuum (open points), and 1D PSF (gray line) on a logarithmic axis; and observed H α velocities along the major kinematic axis (black points), fit with an exponential disk model (red line). The axis profiles are extracted along the kinematic PA as denoted by the light blue line overplotted on the velocity map. The photometric PA, as determined by F160W *HST* images, is shown by the pink line. The blue arcs correspond to $\pm 18^\circ$, the average misalignment between photometric and kinematic PAs, while the pink arcs correspond to $\pm 3\sigma$ error on the photometric PA. In the fourth column, the dotted gray velocity curve shows the best-fit exponential disk model with the inclination correction applied. The dashed gray velocity curve shows the intrinsic rotation curve. The associated shaded region shows the error on the rotational velocity, $v_{\text{rot,corr}}$, corrected for both inclination and beam-smearing effects. (Right) Kinematic maps and axis profiles for the compact SFGs in KMOS^{3D}, continued.

et al. 2007; Burkert et al. 2010; Dalcanton & Stilp 2010). In the case of constant isotropic velocity dispersion (Cresci et al. 2009) adopted for this paper, α is defined as twice the ratio of half-light radius to disk radius, $\alpha = 2r_e/r_d = 3.36$, assuming v is measured at $r = r_e$ (Burkert et al. 2010, 2016). We find a range of disk circular velocities, $v_d = 110\text{--}500 \text{ km s}^{-1}$, for the compact SFGs, which follows the underlying KMOS^{3D} SFG population.

Although the kinematic values v_{rot} , $v_{\text{rot,corr}}$, and v_d are calculated from the maximal velocity difference from the extracted 1D velocity profile, an exponential disk rotation curve is fit for illustrative purposes to the observed 1D velocity profile shown by the red line in Figure 5. The disk scale length of the model curve is constrained to be within 2σ errors of the H α or [O III] half-light radius. The emission-line half-light sizes provide a better prior to obtain a best fit to the observed velocity data in the majority of galaxies. When the radius is left as a free parameter in the rotation-curve fit, the resulting radii

are more closely matched to the H α sizes than the *HST* H-band sizes. Both sizes are shown by vertical lines in the third column of Figure 5.

A further consequence of the small characteristic sizes and morphologies of the compact SFGs is large uncertainties from both the beam-smearing corrections and the $\sin i$ corrections to the observed velocity or line width. As a result of these corrections, the errors on the disk circular velocity for the compact SFGs are large. Even when rotation is resolved, the measured v_{obs} is a lower limit. Corrections for inclination, $(\sin i)^{-1}$, are >2 for nine compact SFGs due to the high axis ratios characteristic of compact SFGs. For galaxies with axis ratios very close to unity, the true inclination correction is highly uncertain. This uncertainty is propagated to v_d ; however, the $\sim 4\text{--}10\%$ errors on the axis ratio may be underestimated for the compact sources presented in this work. In Figure 5, the dotted line shows the inclination correction applied to the best-fit model curve to the observed data.

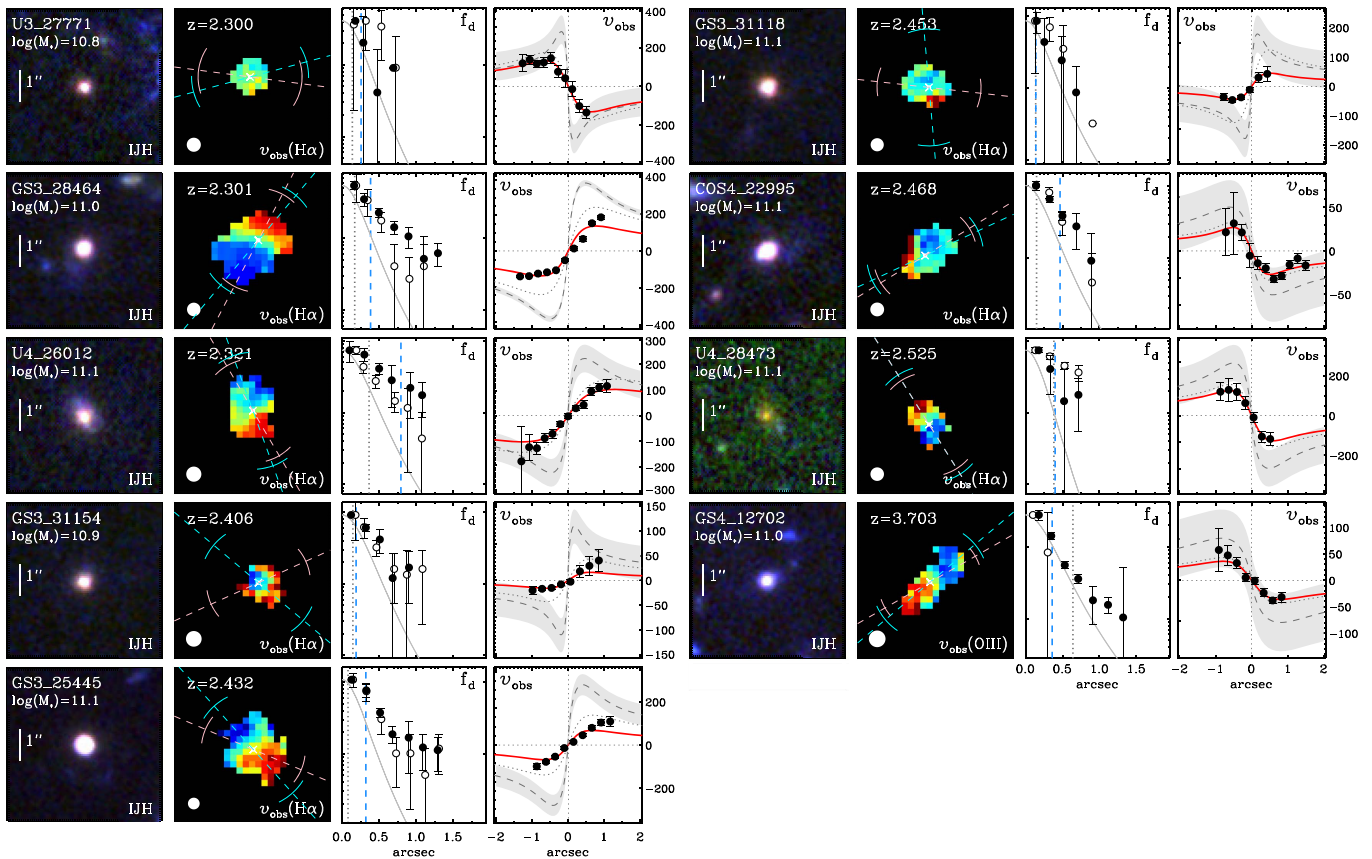


Figure 5. (Continued.)

A beam-smearing correction is applied to the observed velocity, v_{obs} , in addition to the inclination correction. The beam-smearing corrections depend on the ratio of the H -band effective radius to the KMOS PSF. As a result, galaxies with compact H -band sizes have large correction factors. In Figure 5, the intrinsic non-beam-smear rotation curve, assuming the exponential disk radius is equal to $r_c[\text{F160W}]/1.68$, is shown by the dashed line. The average velocity beam-smearing correction factor is 1.5, with a range from 1.2 to 1.9. However, as discussed, inferred intrinsic $H\alpha$ sizes can be 1–4 \times greater than the H -band sizes. In these cases, the beam-smearing corrections may be overestimated when using the H -band size. Beam-smearing corrections are calculated using the $H\alpha$ size for 6/23 resolved galaxies in the sample corresponding to the galaxies with $H\alpha$ sizes 2σ larger than their H -band sizes. For these five galaxies, the intrinsic non-beam-smear rotation curve assumes that the exponential disk radius is equal to $r_{H\alpha}/1.68$. The gray region surrounding the dashed line reflects the errors on the observed velocity, inclination correction, and beam-smearing corrections.

Errors on the beam-smearing corrections are estimated from Monte Carlo simulations of the galaxy parameters that enter into the beam-smearing calculations. For the velocity beam-smearing correction, only the half-light radius is varied. The resulting 34 and 68 percentile errors on the velocity beam-smearing correction are small, typically a few percent. The dominant correction to the velocity is galaxy dependent, as can be seen from the variety of rotation curves in Figure 5. Beam-smearing corrections to σ_0 are dependent on M_* , i , and r_c , as

detailed in Appendix A.2.4 of Burkert et al. (2016). Multiplicative corrections range from 0.2 to 0.9. The 34 and 68 percentile errors on the dispersion beam-smearing correction are larger, typically 40%.

A higher fraction of the compact galaxies may be rotating, but observations are limited by beam size and low surface brightness (despite pushing to low flux levels for many cases, $\sim 4 \times 10^{-18} \text{ erg s}^{-1} \text{ cm}^{-2} \text{ arcsec}^{-2}$ using integration times > 8 hr). Deep AO-assisted data (updating previously seeing-limited observations) of small SFGs have revealed that previously classified dispersion-dominated SFGs ($v_{\text{rot}}/\sigma_0 < 1$) are actually rotationally supported (Newman et al. 2013). Initial observations of compact SFGs yielded large line widths, $\sigma_{\text{tot}} \sim 200\text{--}300 \text{ km s}^{-1}$ (Barro et al. 2014b; Nelson et al. 2014), in some cases interpreted under the assumption that compact SFGs have negligible rotation (Barro et al. 2014b). Recent results, also from the 3D-*HST* sample (van Dokkum et al. 2015), find a wide range of line widths and argue that rotation likely does provide the majority of dynamical support for these galaxies. We directly measure with integral field spectroscopy a similar but wider range of rotational velocities than those in van Dokkum et al. (2015). Compact SFGs have axis ratios close to unity, resulting in poorly constrained photometric axes. An advantage of resolved spectroscopy for these galaxies is that the kinematic axis can be measured independent of the photometric axis. Approximately half, 11/21, of the rotation-dominated compact SFGs have a kinematic misalignment from the photometric axis of $> 30^\circ$, as seen by the blue and pink lines in the second column of Figure 5.

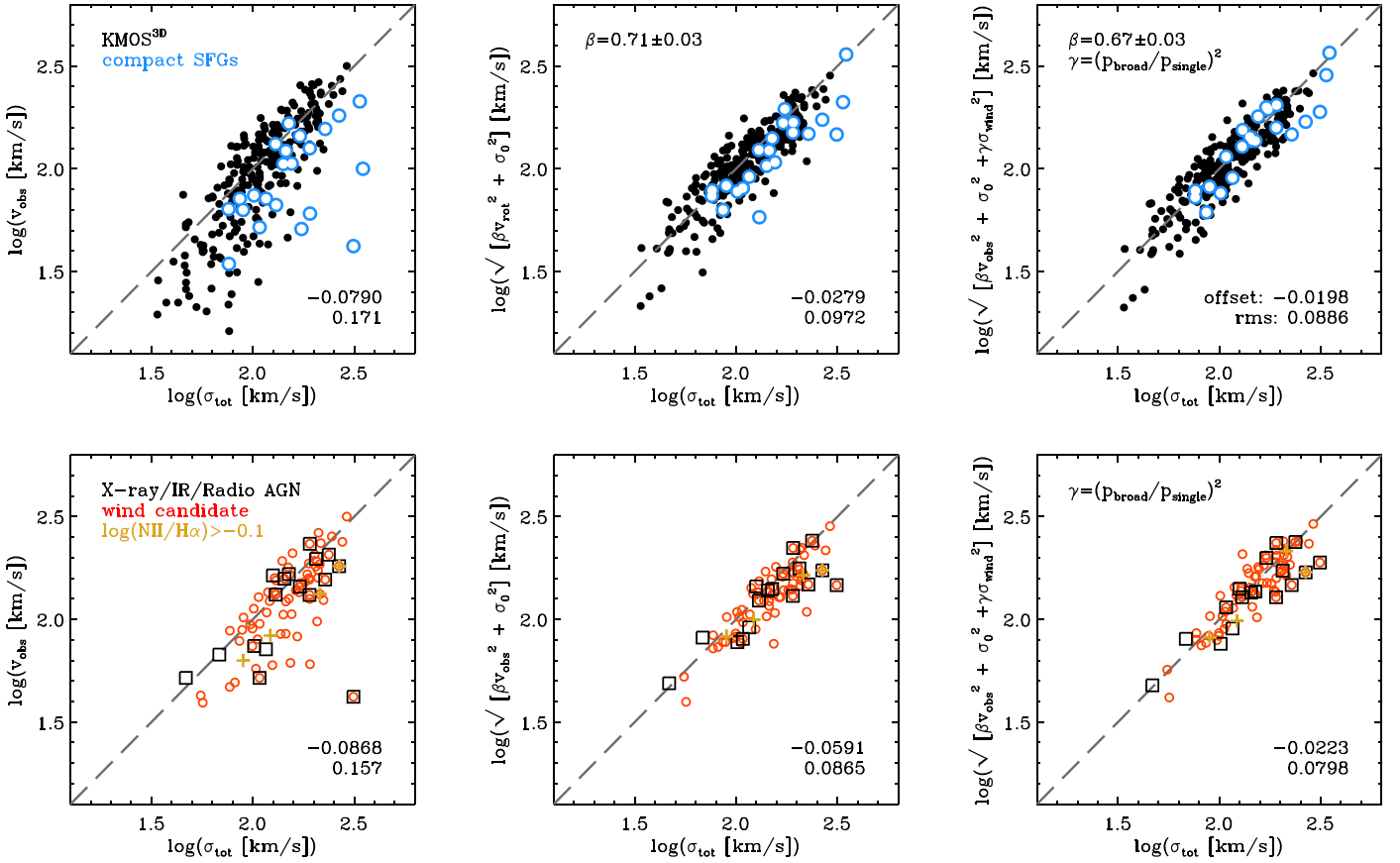


Figure 6. Combinations of resolved kinematic parameters compared to the observed galaxy-integrated line widths using Equation (2). The top panels show the full sample of KMOS^{3D} galaxies that have rotation with obvious pairs and mergers removed (black symbols). Compact SFGs are identified in blue. The bottom panels show the same comparisons for only the candidate AGN host galaxies as selected by X-ray/IR/radio techniques (black squares; see Genzel et al. 2014b; N. M. Förster Schreiber et al. 2018, in preparation), the presence of a secondary broad H α component from the central regions (red circles), or with $\log(\text{N II}/\text{H}\alpha) > -0.1$ (orange crosses). The numbers in the bottom right corner of each panel give the mean offset and scatter in dex, respectively.

3.4. The Dynamics of Integrated Line Widths

As discussed in Section 3.2, the measured integrated emission-line width represents the total dynamics of the system including both rotation and dispersion, as well as nongravitational effects such as galactic-scale winds. With the resolved information from KMOS, we decompose the relative contributions from turbulence, rotation, and large-scale winds to the measured σ_{tot} of compact and extended SFGs with direct measurements.

In theory, the observed line width should be a linear combination of these components, such that

$$\sigma_{\text{tot}} \approx \sqrt{\beta v_{\text{obs}}^2 + \sigma_{\text{ISM}}^2 + \gamma \sigma_{\text{wind}}^2} \quad (2)$$

(e.g., Tully & Fouque 1985; Weiner et al. 2006; van Dokkum et al. 2015). In Equation (2), β is a constant that we calibrate below; σ_{ISM} is the dispersion of the interstellar medium of the galaxy, here approximated by σ_0 ; and σ_{wind} is the dispersion of broad underlying emission from a large-scale wind scaled by factor γ . The functional form of γ is unknown, with a likely dependence on galaxy inclination and wind opening angle. In the absence of knowledge of the detailed structure of the winds, we parameterize γ empirically as the square of the ratio of the peak of the broad component in a two-Gaussian fit to the peak of a single Gaussian fit. This is based on the assumption that the closer the ratio is to unity, the larger the effect of the wind

on the total line width. Here, in contrast to Equation (1), the ISM turbulence, measured as σ_0 , is added in quadrature with no scale factor, reflecting its contribution to line broadening, and no beam-smearing correction is applied. Thus, in the case of a purely face-on disk with no winds, the integrated line width is equivalent to the isotropic disk velocity dispersion, as both observables v_{obs} and σ_{tot} are affected by inclination.

In Figure 6, we test the validity of Equation (2) for $z \approx 1-3$ KMOS^{3D} galaxies showing rotation (disk criterion 1). In the top left panel of Figure 6, we show the measured velocity difference, v_{obs} , as a function of the observed line width, σ_{tot} , for compact SFGs as they relate to the full population of KMOS^{3D} galaxies. While the full sample shows a general agreement at high observed velocities and line widths, there is significant scatter with a tendency for the velocity shear to represent only a fraction of the line width for both the compact SFGs and the full population. This is unsurprising, as local gas velocity dispersions are known to be high at these redshifts (e.g., Förster Schreiber et al. 2006, 2009; Genzel et al. 2006; Law et al. 2007; Cresci et al. 2009; Kassin et al. 2012; Newman et al. 2013; Stott et al. 2016; W15). Adding the turbulent motions in quadrature to the observed velocity difference (top middle panel) reduces the rms comparison to the observed line width for the full KMOS^{3D} sample of rotating galaxies from 0.171 to 0.097 dex with a best-fit scale factor of $\beta = 0.71 \pm 0.03$. Accounting for turbulence is fractionally most

important in systems with a low v_{obs} of 100 km s^{-1} or less, including near face-on objects and galaxies with $v/\sigma \sim 1$ –2.

The rightmost panels of Figure 6 show the comparison with observed integrated line width when the contribution of an additional nongravitational component is considered. For galaxies in our sample with strong broad components, we make a two-Gaussian fit to the rotation-corrected integrated spectrum to determine the contribution from nuclear- or SF-driven winds to the integrated line width (Förster Schreiber et al. 2014; Genzel et al. 2014b; N. M. Förster Schreiber et al. 2018, in preparation). For the strongest cases, an additional broad Gaussian component, σ_{wind} , produces a significant improvement to the overall model spectral fit. Using a conservative cut, we measure σ_{wind} in 68 galaxies, a quarter of our sample, that also have σ_0 and v_{obs} measurements. We see a further reduction of scatter in Figure 6 when taking the wind component into account, with the ratio of the peak emission of the broad and single components $\gamma = (p_{\text{broad}}/p_{\text{single}})^2$ and a best-fit scale factor of $\beta = 0.67 \pm 0.03$. Although the overall effect is small for the full resolved KMOS^{3D} sample, the importance for the compact SFGs can be seen from the offset in the top middle and right panels of Figure 6.

The bottom panels of Figure 6 show the same line-width comparisons for only AGN candidates using all available AGN indicators. The wind term of Equation (2) with scale factor γ is particularly important for the subsample of galaxies that show evidence of hosting nuclear-driven outflows, many of which are classified as compact SFGs. For the galaxies possibly hosting AGNs, we see comparable trends as for the full rotation-dominated sample with a reduction in scatter from 0.087 to 0.080 dex when including the contributions from winds, indicating that the presence of an AGN could influence the derived 1D kinematics as seen from the spectra shown in Figure 3 of COS4_11363, for example.

The velocity scale factor, β , in Equation (2) reflects the projection of the rotational velocity along the line of sight with literature values ranging from 0.5 to 0.75 (e.g., Rix et al. 1997; Erb et al. 2006; Weiner et al. 2006; Zolotov et al. 2015). We use our observables to solve for the value of $\beta = 0.67 \pm 0.03$, which brings the left and right sides of Equation (2) into agreement for the KMOS^{3D} data as shown in the rightmost panels of Figure 6. If the wind component is not considered (middle panels), then β is slightly lower but consistent within the uncertainties, 0.71 ± 0.03 . This value is higher than that typically used by previous studies; however, β may encompass a mix of dependencies on aperture size, line-profile asymmetries, beam smearing, centrally weighted light profiles, and magnitude of random motions (Rix et al. 1997) and thus may be sample- or data-specific.

The exact form of Equations (1) and (2) and the constant α in Equation (1) are dependent on the radial distribution of density and velocity dispersion assumed. For a spherically symmetric system with isotropic velocity dispersion, $v = \sqrt{2} \sigma$ or $v = \sqrt{3} \sigma$, depending on the exact model used (Binney & Tremaine 2008). This formalism motivates the $S_{0.5}$ dynamical parameter popularized for use in Tully–Fisher analyses (e.g., Weiner et al. 2006; Kassin et al. 2007; Cortese et al. 2014). Setting $\beta = 0.5$ here produces a similar reduction in scatter (rms = 0.0995) but leads to a larger offset with 78% of values having $\sigma_{\text{tot}} > S_{0.5}$ (offset = -0.0756).

A caveat is that in small or faint galaxies in which the KMOS observations do not probe to the outer regions of the

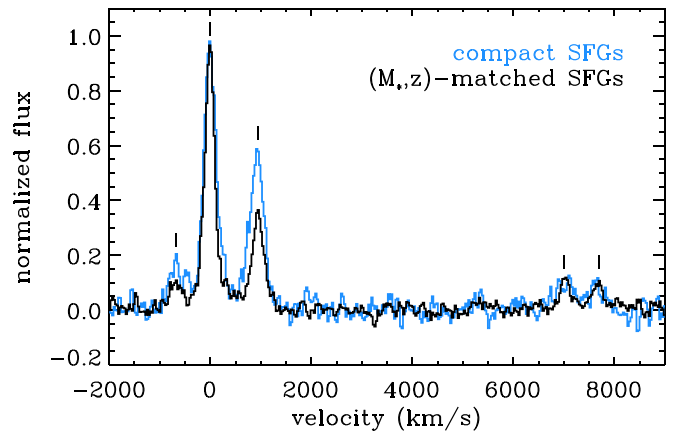


Figure 7. Stacked KMOS spectra for 23 compact SFGs (blue) and a stellar mass and redshift-matched comparison sample of 46 galaxies from KMOS^{3D} (black). The velocity axis is centered around H α . The positions of H α , [N II] $\lambda\lambda 6548, 6584$, and [S II] $\lambda\lambda 6717, 6731$ are identified with vertical lines.

disk, the v_{obs} values may be biased low and the σ_0 values may be biased high. However, the dual measurement effects act together, minimizing their effect (Covington et al. 2010).

3.5. Integrated Line Ratios

We measure a wide range of $\log([\text{N II}]/\text{H}\alpha)$ ratios, -0.5 to 0.2 , for compact SFGs as shown in Figure 3. We combine the spectra in a median stack of H α -normalized spectra to determine the average emission-line properties of compact SFGs. By stacking, we are able to detect the weaker lines [S II] $\lambda\lambda 6717, 6731$. Broad-line AGNs are removed prior to stacking. For comparison, a mass and redshift-matched stack is also produced, drawing from the full KMOS^{3D} sample. Both stacked spectra are shown in Figure 7. The residuals from a single-component Gaussian fit to the H α -[N II]-[S II] lines reveal excess emission, especially near the H α -[N II] complex. This emission is likely from stellar or nuclear-driven winds, as discussed above. For simplicity, we adopt a single-component fit to the emission lines. However, we note that the narrow component for a two-component fit is consistent within 2σ errors with the single-component fit.

The compact SFGs (blue spectrum in Figure 7) show a higher [N II]/H α ratio, 0.58 ± 0.2 , than the mass and redshift-matched comparison sample (black spectrum), 0.38 ± 0.1 , while the [S II]/H α ratios are consistent within the errors, 0.21 ± 0.2 and 0.22 ± 0.1 , respectively. The high [N II]/H α ratios are expected given the high AGN fraction in massive galaxies and, particularly, the compact SFGs, as discussed in the previous section. The low [S II]/H α ratios in both stacks may be the result of a higher ionization parameter (Brinchmann et al. 2008; Kewley et al. 2015; Kashino et al. 2017) and are inconsistent with pure shock or LINER-driven emission (from local calibrations; Rich et al. 2011).

3.6. Dynamical Mass

We estimate the dynamical mass, M_{dyn} , assuming a thick (1:4) exponential disk for the KMOS^{3D} rotation-dominated galaxies (disk criterion 1 and 2) from the rotational velocities using

$$M_{\text{dyn}}^d(r < r_e) = \frac{v_d^2 r_e}{\alpha_0 G}, \quad (3)$$

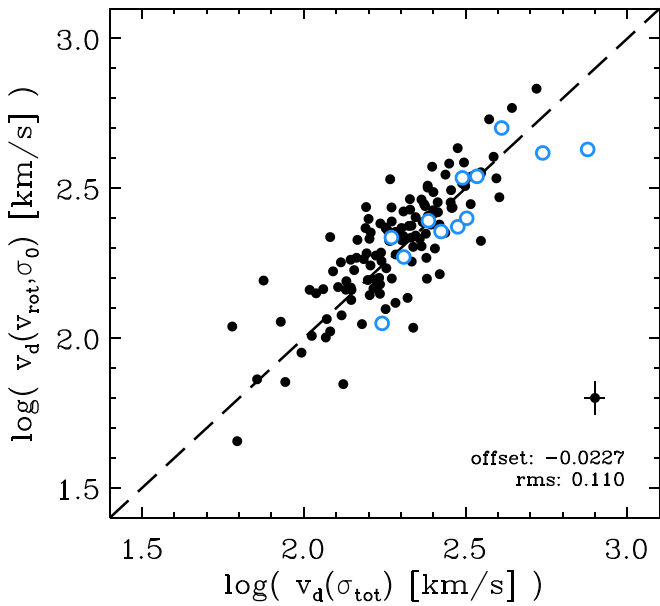


Figure 8. Disk circular velocity derived from the resolved kinematic parameters, v_{rot} and σ_0 , vs. the disk circular velocity derived from the integrated line width using Equation (4). Symbols are the same as in Figure 6. A representative error bar is shown in the bottom right corner.

where the factor α_0 is dependent on the mass distribution of the system (Binney & Tremaine 2008). We assume $\alpha = 1.09$ for a pressure-supported thick disk. We use the half-light sizes, r_e , measured from observed F160W H -band light from the CANDELS imaging using single Sérsic fits (Lang et al. 2014). For a full analysis of the baryon fractions of KMOS^{3D} galaxies and a 2D modeling approach, see Wuyts et al. (2016). The dynamical mass estimates would marginally increase if H α half-light sizes were used for the full sample, as $r_{\text{H}\alpha}/r_e$ is close to unity for the majority of SFGs at this epoch (Nelson et al. 2014; D. Wilman et al. 2018, in preparation).

For galaxies with unresolved kinematics, we estimate the disk circular velocity from the observed line width, under the assumption that their dynamics are dominated by rotation (Binney & Tremaine 2008). Because disk velocity dispersions are high at these epochs, proving nonnegligible pressure support, Equation (2) alone is not sufficient to derive the velocity. Thus, to derive the disk circular velocity from the integrated line width, the corrections take the composite form of

$$v_d = \sqrt{\frac{(\sigma_{\text{tot}}^2 - \sigma_0^2 - \gamma\sigma_{\text{wind}}^2)}{\beta \sin^2 i}} + 3.36\sigma_0. \quad (4)$$

However, Equation (4) requires knowledge of σ_0 and σ_{wind} , which are not available in the unresolved case. We estimate σ_0 based solely on redshift, such that $\sigma_0 \sim 25 \text{ km s}^{-1}$ at $z < 1.2$, $\sigma_0 \sim 35 \text{ km s}^{-1}$ at $1.2 < z < 1.8$, and $\sigma_0 \sim 50 \text{ km s}^{-1}$ at $z > 1.8$ (W15), and assume that $\sigma_{\text{wind}} = 0$. We test this method on resolved rotation-dominated galaxies, shown in Figure 8, finding reasonable agreement between v_d estimated from resolved parameters in Equation (1) and v_d estimated from Equation (4), $v_d(v_{\text{rot}}, \sigma_0)/v_d(\sigma_{\text{tot}}) = 1.15$ with 0.11 dex scatter. A large portion of the scatter is likely due to the range in measured σ_0 values at each epoch (W15).

We also test the simpler case, in which we assume that the turbulence and wind contributions are negligible and only apply an inclination correction to σ_{tot} . The comparison between

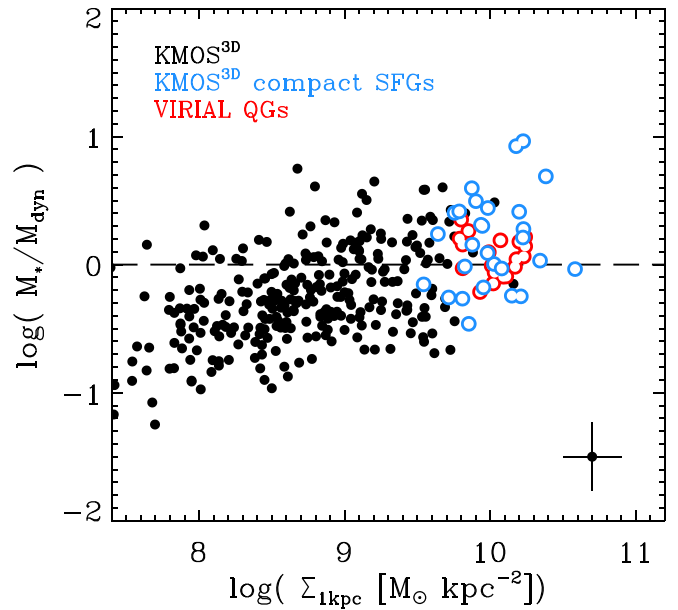


Figure 9. Stellar-to-dynamical mass fraction as a function of inner kpc density for extended SFGs, compact SFGs, and quiescent galaxies. Dynamical masses are estimated from Equation (3) for SFGs and from JAM modeling for quiescent galaxies from the VIRIAL survey (Mendel et al. 2015; J. T. Mendel 2018, in preparation). A representative 1σ error bar is shown in the bottom right corner.

inclination-corrected σ_{tot} and v_d shows, on average, that $v_d \sim 1.31(\sigma_{\text{tot}}/\sin i)$ for the full sample. Although less physically motivated, the rms scatter for this method is comparable to using the method described above.

In Figure 9, we investigate the relationship between stellar and dynamical mass as a function of inner kpc density recovering a weak trend, such that the most centrally dense objects, including compact SFGs and quiescent galaxies, have stellar mass fractions closest to unity. We compare our results to the VIRIAL survey of quiescent galaxies. In contrast, their dynamical masses are computed from a combination of stellar kinematics and photometry with Jeans Anisotropic Models (JAM) modeling (Cappellari 2008). With this comparison sample, we find that compact SFGs are consistent with quiescent galaxies in both central density and stellar baryon fraction with M_*/M_{dyn} scattered around unity. This implies that there is little room for a significant additional mass component from molecular gas, atomic gas, or dark matter within the regions of the galaxies probed by our measurements. The high stellar-to-dynamical mass ratios and high stellar densities suggest a short timescale for the onset of quenching. Indeed, recent CO and [C I] ALMA observations of compact SFGs GS3_19791 and COS4_22995, also in our sample, reveal a molecular gas fraction between 4% and 14%, as well as short depletion times (Spilker et al. 2016; Popping et al. 2017). These gas fractions are consistent with the gas fractions implied by the ratio of the dynamical mass estimates and stellar masses. They are significantly lower than the average gas fractions of “typical” $z \sim 2$ extended SFGs of $\gtrsim 40\%$ (Daddi et al. 2010; Tacconi et al. 2010, 2013, 2018; Genzel et al. 2015).

As discussed in Wuyts et al. (2016), some galaxies scatter to unphysical baryon fractions. We investigate this further for the specific case of compact SFGs, looking for trends with galaxy properties. Inclination corrections are particularly uncertain for

compact SFGs, as the typical axis ratios are close to unity. They are difficult to measure due to both the circular appearance of the galaxies and their small size in comparison to the *HST* PSF. The compact SFG with the highest stellar baryon fraction has an axis ratio of $q \sim 0.6$. If the axis ratio was increased to $q = 1$, comparable with other compact SFGs of the sample, then $\log(M_*/M_{\text{dyn}})$ would be reduced to -0.3 , in line with the scatter of the rest of the population.

4. Discussion

Compact SFGs have garnered a lot of attention in the last 5 years as a possible transitional population between the massive end of the star-forming MS and the quiescent galaxy population (e.g., Barro et al. 2013, 2014a, 2014b; Dekel & Burkert 2014; Tadaki et al. 2014; Williams et al. 2014; Brennan et al. 2015). Two dominant theories have emerged as to how compact SFGs are formed: either through gas dissipation and a central starburst (Dekel & Burkert 2014; Tadaki et al. 2017a) or from already small less-massive SFGs (van Dokkum et al. 2015; Lilly & Carollo 2016). In contrast, compact SFGs have been universally linked as the immediate progenitors of compact quiescent galaxies at $z \sim 1-2$ and thus the likely progenitors of a fraction of S0 or elliptical galaxies in the local universe. We explore our resolved $H\alpha$ results in the context of these scenarios.

4.1. Forming Compact SFGs

In the ‘‘compaction’’ formation scenario, central starbursts within extended galaxies rapidly build up a central mass concentration, creating the possible precursors of compact SFGs. Tadaki et al. (2017b) presented two such galaxies at $z = 2.5$ with dust-obscured cores and compact molecular gas sizes (~ 1.3 kpc). The starburst cores have sizes, v_{rot}/σ , and v_{rot} comparable to our $H\alpha$ results of compact SFGs. However, it follows that a more extended stellar disk remains that may be obscured or outshined by the central core. The measured $H\alpha$ profiles of KMOS^{3D} compact SFGs with exponential disks of $r_{H\alpha} \sim 2.5 \pm 0.2$ kpc and high stellar baryon fractions suggest that we are unlikely to be missing substantially larger extincted star-forming disks.

Alternatively, the $H\alpha$ and continuum sizes may more simply suggest that compact SFGs are among the oldest galaxies in our full SFG population, such that their current small observed sizes are reflective of the average population at the epoch when they assembled the bulk of their stellar mass (e.g., van Dokkum et al. 2015; Lilly & Carollo 2016). In this scenario, dissipative processes may still have been responsible for creating the high central density but may have done so on a different timescale than the central starburst scenario.

4.2. Compact SFGs as Progenitors of Compact Quiescent Galaxies

The high stellar-to-dynamical mass ratios measured for the KMOS^{3D} compact SFGs imply that the onset of quenching of the remaining star formation should be fast, as there is little room for molecular gas reservoirs. Further support for short timescales comes from the morphology of compact SFGs (e.g., bulge-to-total ratios $B/T \sim 0.5$ and Sérsic indices $n \sim 3$). Galactic structure, both locally and at $z \sim 1-2$, has been linked to high passive fractions for massive galaxies (Kauffmann et al. 2003b; Driver et al. 2006; Wuyts et al. 2011b; Bell et al. 2012).

The results presented here and in other KMOS^{3D} papers (Burkert et al. 2016; Wuyts et al. 2016) are consistent with scenarios in which SFGs approach a critical mass or mass density before quenching.

Our kinematic results reveal that $>50\%$ of compact SFGs have a disk component with significant rotational support. If compact SFGs are the true progenitors of quiescent galaxies, then the quenching process at this epoch will either destroy the rotation, leaving a pressure-supported quiescent galaxy, or leave the rotation intact, forming a rotating quiescent galaxy. In the second scenario, the disklike kinematics and large disk circular velocities imply that compact quiescent galaxies would be observed as ‘‘fast rotators’’ at later times. Evidence of rotating quiescent galaxies at $z \gtrsim 1$ from the literature includes observational results from deep imaging that suggest as many as $\gtrsim 65\%$ of compact quiescent galaxies are disk-dominated at $z \sim 2$ (van Dokkum et al. 2008; van der Wel et al. 2011; Chevance et al. 2012) and spectroscopic results of two strongly lensed $z > 2.1$ quiescent galaxies that reveal stellar rotation curves of $V_{\text{max}} \approx 190$ and $V_{\text{max}} \approx 500$ km s⁻¹ (Newman et al. 2015; Toft et al. 2017). The rotation detected in both compact SFGs and quiescent galaxies implies that integrated σ_* measurements of quiescent galaxies likely have a rotational component (see also Belli et al. 2017b; J. T. Mendel et al. 2018, in preparation).

The dynamics of local descendants of rotating high-redshift compact galaxies depends strongly on their accretion histories. High-redshift compact galaxies may evolve into kinematically distinct cores, compact galaxies, or S0s (e.g., Cappellari 2016). It is possible that they become the fast rotators observed in high fractions locally (50%–95% of galaxies with $10 < \log M_*/[M_\odot] < 11$; e.g., Emsellem et al. 2011; van de Sande et al. 2017; Greene et al. 2018). However, the stellar masses could still increase by almost an order of magnitude from $z \sim 2-3$ to today (e.g., Muzzin et al. 2013). If the compact SFGs follow this path, they may lose angular momentum due to merging and evolve into slow rotators at the highest masses (e.g., $\log M_*/[M_\odot] > 11$; Wellons et al. 2016).

Merging is a possible mechanism to quench existing compact SFGs (e.g., Wellons et al. 2015; Zolotov et al. 2015), which could either destroy or retain the existing rotational support (Naab & Burkert 2003; Hammer et al. 2005; Wuyts et al. 2010). There are two possible major mergers (mass ratios of 1:1, 1:2) in our sample identified by spectroscopic redshifts and projected separations (< 300 km s⁻¹, < 14 kpc). However, the number of possible companions around compact SFGs within 1σ redshift errors and 50 kpc (drawing from the 3D-*HST* catalog) is consistent within the errors with the full SFG sample of massive galaxies, $\log(M_*/[M_\odot]) > 10$, in KMOS^{3D}, suggesting that major mergers are not the sole mechanism responsible for quenching compact SFGs.

AGNs provide another mechanism to quench galaxies, particularly at these masses and redshifts (e.g., Di Matteo et al. 2005; Croton et al. 2006; Hopkins et al. 2006; Shimizu et al. 2015), and have been proposed specifically for compact SFGs as a likely quenching mechanism (Barro et al. 2013). With access to additional metrics to measure nuclear activity ($[\text{N II}]/H\alpha$ ratios and deep data to recover broad underlying emission components), we have found an even higher rate of possible AGN activity in compact SFGs. We estimate that the

AGN incidence is $\sim 1.4\times$ higher in compact SFGs than in the overall population at a fixed stellar mass. While we cannot rule out that this is partially a consequence of selection due to the emission from an AGN being attributed to star formation or an AGN outshining a large underlying disk, it is suggestive that AGNs may play a central role in the evolutionary tracks of compact SFGs. The high [N II]/H α emission-line ratio in the compact SFG stack is consistent with emission-line ratios found in quiescent galaxies both locally (Yan et al. 2006) and at high redshift (Newman et al. 2015; Belli et al. 2017a; Toft et al. 2017).

5. Conclusions

We present the kinematic properties of 35 compact centrally dense SFGs at $z = 0.9\text{--}3.7$ in the KMOS^{3D} survey. For the first time with integral field spectroscopy, we spatially resolve 23 compact SFGs. The integral field spectroscopy data map the emission-line kinematics and morphology in two spatial dimensions, enabling a determination of the kinematic position angle in rotating galaxies. The data reveal that the majority of resolved compact SFGs, 21/23, are rotationally dominated systems with rotational velocities and disk dispersions comparable to the full KMOS^{3D} data set of SFGs at similar masses. With the kinematic position angle, now we can measure velocity gradients ranging from 95 to 500 km s⁻¹. The integrated ionized gas line widths of compact SFGs (75–400 km s⁻¹) and extended SFGs can be reproduced by a combination of their observed rotation, disk velocity dispersion, and wind strength. This line decomposition demonstrates the important interplay of the different kinematic components of these systems when inferring rotational velocities from unresolved data.

The H α profiles of compact SFGs are well fit with an exponential disk model with a size of ~ 2 kpc, slightly larger or comparable to the broadband continuum sizes. This result and the detection of rotation are in line with earlier results presented by van Dokkum et al. (2015). Stacked spectra of compact SFGs show higher [N II]/H α and comparable [S II]/H α to a stellar mass and redshift-matched sample.

We derive large dynamical masses, leaving little room for large molecular gas reservoirs—a result supported by recent ALMA observations of two of the compact SFGs in our sample. The high M_*/M_{dyn} ratios together with the structural parameters (high central densities and cuspy profiles) suggest that, assuming no further gas replenishment, these galaxies will have their large SFRs quenched on a short timescale. Depending on the quenching mechanism, it is possible that the resultant quiescent galaxies would retain the rotational support observed in the compact SFG phase. There is a growing amount of evidence in the literature to support the scenario of rotationally supported quiescent galaxies at $z \sim 0.5\text{--}3$. Integrated ionized gas line widths of compact SFGs are comparable to the stellar velocity dispersions of compact quiescent galaxies at similar redshifts. However, direct measurement of stellar and gas velocity dispersions in the same objects (e.g., Barro et al. 2016) for a large sample is required to see if a link between these two measurements can be made, on average. Future work utilizing synergies between the KMOS^{3D} survey and the complementary VIRIAL survey (Mendel et al. 2015) of UVJ passive galaxies in the same fields will investigate the relationship between stellar and ionized gas line widths for a sample of galaxies observed in both surveys.

We wish to thank the ESO staff, in particular the staff at Paranal Observatory, for their helpful and enthusiastic support during the many observing runs over which the KMOS GTO was carried out. We thank the entire KMOS instrument and commissioning team for their hard work. We also thank the software development team of SPARK for all their work with us to get the most out of the data. DJW and MF acknowledge the support of the Deutsche Forschungsgemeinschaft via Project IDs 3871/1-1 and 3871/1-2. EW acknowledges the support of ASTRO 3D funding for the writing retreat used to bring this paper to completion. Parts of this research were conducted by the Australian Research Council Centre of Excellence for All Sky Astrophysics in 3 Dimensions (ASTRO 3D) through project number CE170100013.

ORCID iDs

J. T. Mendel  <https://orcid.org/0000-0002-6327-9147>
 N. M. Förster Schreiber  <https://orcid.org/0000-0003-4264-3381>
 R. Genzel  <https://orcid.org/0000-0002-2767-9653>
 D. Wilman  <https://orcid.org/0000-0002-1822-4462>
 S. Wuyts  <https://orcid.org/0000-0003-3735-1931>
 S. Belli  <https://orcid.org/0000-0002-5615-6018>
 A. Beifiori  <https://orcid.org/0000-0001-8017-6097>
 R. Bender  <https://orcid.org/0000-0001-7179-0626>
 J. Chan  <https://orcid.org/0000-0001-6251-3125>
 R. L. Davies  <https://orcid.org/0000-0002-3324-4824>
 M. Fossati  <https://orcid.org/0000-0002-9043-8764>
 P. Lang  <https://orcid.org/0000-0002-5681-3575>
 D. Lutz  <https://orcid.org/0000-0003-0291-9582>
 E. J. Nelson  <https://orcid.org/0000-0002-7524-374X>
 I. Momcheva  <https://orcid.org/0000-0003-1665-2073>
 D. Rosario  <https://orcid.org/0000-0002-0001-3587>
 R. Saglia  <https://orcid.org/0000-0003-0378-7032>
 L. J. Tacconi  <https://orcid.org/0000-0002-1485-9401>
 K. Takaki  <https://orcid.org/0000-0001-9728-8909>

References

- Alexander, D. M., Swinbank, A. M., Smail, I., McDermid, R., & Nesvadba, N. P. H. 2010, *MNRAS*, **402**, 2211
- Balogh, M. L., Baldry, I. K., Nichol, R., et al. 2004, *ApJL*, **615**, L101
- Barro, G., Faber, S. M., Dekel, A., et al. 2016, *ApJ*, **820**, 120
- Barro, G., Faber, S. M., Pérez-González, P. G., et al. 2013, *ApJ*, **765**, 104
- Barro, G., Faber, S. M., Pérez-González, P. G., et al. 2014a, *ApJ*, **791**, 52
- Barro, G., Trump, J. R., Koo, D. C., et al. 2014b, *ApJ*, **795**, 145
- Beifiori, A., Mendel, J. T., Chan, J. C. C., et al. 2017, *ApJ*, **846**, 120
- Bell, E. F., van der Wel, A., Papovich, C., et al. 2012, *ApJ*, **753**, 167
- Belli, S., Newman, A. B., & Ellis, R. S. 2014, *ApJ*, **783**, 117
- Belli, S., Genzel, R., Förster Schreiber, N. M., et al. 2017a, *ApJL*, **841**, L6
- Belli, S., Newman, A. B., & Ellis, R. S. 2017b, *ApJ*, **834**, 18
- Best, P. N., Kauffmann, G., Heckman, T. M., et al. 2005, *MNRAS*, **362**, 25
- Bezanson, R., Franx, M., & van Dokkum, P. G. 2015, *ApJ*, **799**, 148
- Binney, J., & Tremaine, S. 2008, *Galactic Dynamics* (2nd ed.; Princeton, NJ: Princeton Univ. Press)
- Bluck, A. F. L., Mendel, J. T., Ellison, S. L., et al. 2014, *MNRAS*, **441**, 599
- Bournaud, F., Elmegreen, B. G., & Elmegreen, D. M. 2007, *ApJ*, **670**, 237
- Bower, R. G., Benson, A. J., Malbon, R., et al. 2006, *MNRAS*, **370**, 645
- Brammer, G., van Dokkum, P., Franx, M., et al. 2012, *ApJS*, **200**, 13
- Brennan, R., Pandya, V., Somerville, R. S., et al. 2015, *MNRAS*, **451**, 2933
- Brinchmann, J., Pettini, M., & Charlot, S. 2008, *MNRAS*, **385**, 769
- Brusa, M., Fiore, F., Santini, P., et al. 2009, *A&A*, **507**, 1277
- Bundy, K., Georgakakis, A., Nandra, K., et al. 2008, *ApJ*, **681**, 931
- Burkert, A., Förster Schreiber, N. M., Genzel, R., et al. 2016, *ApJ*, **826**, 214
- Burkert, A., Genzel, R., Bouché, N., et al. 2010, *ApJ*, **725**, 2324
- Cappellari, M. 2008, *MNRAS*, **390**, 71
- Cappellari, M. 2016, *ARA&A*, **54**, 597

- Cappellari, M., Bacon, R., Bureau, M., et al. 2006, *MNRAS*, 366, 1126
- Cappellari, M., Emsellem, E., Krajnovic, D., et al. 2011, *MNRAS*, 416, 1680
- Cappellari, M., McDermid, R. M., Alatalo, K., et al. 2013, *MNRAS*, 432, 1862
- Chabrier, G. 2003, *PASP*, 115, 763
- Chang, Y.-Y., van der Wel, A., Rix, H.-W., et al. 2013, *ApJ*, 773, 149
- Cheung, E., Faber, S. M., Koo, D. C., et al. 2012, *ApJ*, 760, 131
- Chevance, M., Weijmans, A.-M., Damjanov, I., et al. 2012, *ApJL*, 754, L24
- Cortese, L., Fogarty, L. M. R., Ho, I.-T., et al. 2014, *ApJL*, 795, L37
- Courteau, S., Cappellari, M., de Jong, R. S., et al. 2014, *RvMP*, 86, 47
- Covington, M. D., Kassin, S. A., Dutton, A. A., et al. 2010, *ApJ*, 710, 279
- Craun, R. A., Schaye, J., Bower, R. G., et al. 2015, *MNRAS*, 450, 1937
- Cresci, G., Hicks, E. K. S., Genzel, R., et al. 2009, *ApJ*, 697, 115
- Croton, D. J., Springel, V., White, S. D. M., et al. 2006, *MNRAS*, 365, 11
- Daddi, E., Bournaud, F., Walter, F., et al. 2010, *ApJ*, 713, 686
- Dalcanton, J. J., & Stilp, A. M. 2010, *ApJ*, 721, 547
- Damjanov, I., McCarthy, P. J., Abraham, R. G., et al. 2009, *ApJ*, 695, 101
- Dekel, A., & Burkert, A. 2014, *MNRAS*, 438, 1870
- Di Matteo, T., Springel, V., & Hernquist, L. 2005, *Natur*, 433, 604
- Driver, S. P., Allen, P. D., Graham, A. W., et al. 2006, *MNRAS*, 368, 414
- Emsellem, E., Cappellari, M., Krajnovic, D., et al. 2007, *MNRAS*, 379, 401
- Emsellem, E., Cappellari, M., Krajnovic, D., et al. 2011, *MNRAS*, 414, 888
- Erb, D. K., Steidel, C. C., Shapley, A. E., et al. 2006, *ApJ*, 646, 107
- Erwin, P. 2015, *ApJ*, 799, 226
- Fang, J. J., Faber, S. M., Koo, D. C., & Dekel, A. 2013, *ApJ*, 776, 63
- Förster Schreiber, N. M., Genzel, R., Bouché, N., et al. 2009, *ApJ*, 706, 1364
- Förster Schreiber, N. M., Genzel, R., Lehnert, M. D., et al. 2006, *ApJ*, 645, 1062
- Förster Schreiber, N. M., Genzel, R., Newman, S. F., et al. 2014, *ApJ*, 787, 38
- Fossati, M., Wilman, D. J., Mendel, J. T., et al. 2017, *ApJ*, 835, 153
- Genel, S., Vogelsberger, M., Springel, V., et al. 2014, *MNRAS*, 445, 175
- Genzel, R., Förster Schreiber, N. M., Lang, P., et al. 2014a, *ApJ*, 785, 75
- Genzel, R., Förster Schreiber, N. M., Rosario, D., et al. 2014b, *ApJ*, 796, 7
- Genzel, R., Tacconi, L. J., Eisenhauer, F., et al. 2006, *Natur*, 442, 786
- Genzel, R., Tacconi, L. J., Lutz, D., et al. 2015, *ApJ*, 800, 20
- Greene, J. E., Leauthaud, A., Emsellem, E., et al. 2018, *ApJ*, 852, 36
- Grogin, N. A., Kocevski, D. D., Faber, S. M., et al. 2011, *ApJS*, 197, 35
- Guerou, A., Krajnovic, D., Epinat, B., et al. 2017, *A&A*, 608, A5
- Hammer, F., Flores, H., Elbaz, D., et al. 2005, *A&A*, 430, 115
- Hopkins, P. F., Bundy, K., Croton, D., et al. 2010, *ApJ*, 715, 202
- Hopkins, P. F., Hernquist, L., Cox, T. J., et al. 2006, *ApJS*, 163, 1
- Kashino, D., Silverman, J. D., Sanders, D., et al. 2017, *ApJ*, 835, 88
- Kassin, S. A., Weiner, B. J., Faber, S. M., et al. 2007, *ApJL*, 660, L35
- Kassin, S. A., Weiner, B. J., Faber, S. M., et al. 2012, *ApJ*, 758, 106
- Kauffmann, G., Heckman, T. M., Tremonti, C., et al. 2003a, *MNRAS*, 346, 1055
- Kauffmann, G., Heckman, T. M., White, S. D. M., et al. 2003b, *MNRAS*, 341, 54
- Kewley, L. J., Zahid, H. J., Geller, M. J., et al. 2015, *ApJL*, 812, L20
- Kocevski, D. D., Barro, G., Faber, S. M., et al. 2017, *ApJ*, 846, 112
- Koekemoer, A. M., Faber, S. M., Ferguson, H. C., et al. 2011, *ApJS*, 197, 36
- Lang, P., Wuyts, S., Somerville, R. S., et al. 2014, *ApJ*, 788, 11
- Law, D. R., Steidel, C. C., Erb, D. K., et al. 2007, *ApJ*, 669, 929
- Lilly, S. J., & Carollo, C. M. 2016, *ApJ*, 833, 1
- Martig, M., Bournaud, F., Teysier, R., & Dekel, A. 2009, *ApJ*, 707, 250
- Martin, D. C., Wyder, T. K., Schiminovich, D., et al. 2007, *ApJS*, 173, 342
- Mendel, J. T., Saglia, R. P., Bender, R., et al. 2015, *ApJL*, 804, L4
- Mihos, J. C., & Hernquist, L. 1994, *ApJL*, 425, L13
- Momcheva, I. G., Brammer, G. B., van Dokkum, P. G., et al. 2016, *ApJS*, 225, 27
- Muzzin, A., Marchesini, D., Stefanon, M., et al. 2013, *ApJ*, 777, 18
- Naab, T., & Burkert, A. 2003, *ApJ*, 597, 893
- Nelson, E., van Dokkum, P., Franx, M., et al. 2014, *Natur*, 513, 394
- Nelson, E. J., van Dokkum, P. G., Förster Schreiber, N. M., et al. 2016, *ApJ*, 828, 27
- Newman, A. B., Belli, S., & Ellis, R. S. 2015, *ApJL*, 813, L7
- Newman, A. B., Ellis, R. S., Bundy, K., & Treu, T. 2012, *ApJ*, 746, 162
- Newman, S. F., Genzel, R., Förster Schreiber, N. M., et al. 2013, *ApJ*, 767, 104
- Peng, C. Y., Ho, L. C., Impey, C. D., & Rix, H.-W. 2002, *AJ*, 124, 266
- Peng, Y.-j., Lilly, S. J., Kovač, K., et al. 2010, *ApJ*, 721, 193
- Popping, G., Decarli, R., Man, A. W. S., et al. 2017, *A&A*, 602, A11
- Reddy, N. A., Erb, D. K., Steidel, C. C., et al. 2005, *ApJ*, 633, 748
- Rich, J. A., Kewley, L. J., & Dopita, M. A. 2011, *ApJ*, 734, 87
- Rix, H.-W., Guhathakurta, P., Colless, M., & Ing, K. 1997, *MNRAS*, 285, 779
- Schaye, J., Craun, R. A., Bower, R. G., et al. 2015, *MNRAS*, 446, 521
- Shapiro, K. L., Genzel, R., Quataert, E., et al. 2009, *ApJ*, 701, 955
- Sharples, R., Bender, R., Agudo Berbel, A., et al. 2013, *Msngr*, 151, 21
- Shimizu, T. T., Mushotzky, R. F., Meléndez, M., Koss, M., & Rosario, D. J. 2015, *MNRAS*, 452, 1841
- Skilton, R. E., Whitaker, K. E., Momcheva, I. G., et al. 2014, *ApJS*, 214, 24
- Spilker, J. S., Bezanson, R., Marrone, D. P., et al. 2016, *ApJ*, 832, 19
- Stott, J. P., Swinbank, A. M., Johnson, H. L., et al. 2016, *MNRAS*, 457, 1888
- Tacchella, S., Dekel, A., Carollo, C. M., et al. 2016, *MNRAS*, 458, 242
- Tacconi, L. J., Genzel, R., Neri, R., et al. 2010, *Natur*, 463, 781
- Tacconi, L. J., Genzel, R., Saitonge, A., et al. 2018, *ApJ*, 853, 179
- Tacconi, L. J., Neri, R., Genzel, R., et al. 2013, *ApJ*, 768, 74
- Tadaki, K.-i., Genzel, R., Kodama, T., et al. 2017a, *ApJ*, 834, 135
- Tadaki, K.-i., Kodama, T., Nelson, E. J., et al. 2017b, *ApJL*, 841, L25
- Tadaki, K.-i., Kodama, T., Tanaka, I., et al. 2014, *ApJ*, 780, 77
- Toft, S., Zabl, J., Richard, J., et al. 2017, *Natur*, 546, 510
- Toomre, A., & Toomre, J. 1972, *ApJ*, 178, 623
- Trujillo, I., Conselice, C. J., Bundy, K., et al. 2007, *MNRAS*, 382, 109
- Tully, R. B., & Fisher, J. R. 1977, *A&A*, 54, 661
- Tully, R. B., & Fouque, P. 1985, *ApJS*, 58, 67
- Übler, H., Förster Schreiber, N. M., Genzel, R., et al. 2017, *ApJ*, 842, 121
- Valenzuela, O., Rhee, G., Klypin, A., et al. 2007, *ApJ*, 657, 773
- van de Sande, J., Bland-Hawthorn, J., Brough, S., et al. 2017, *MNRAS*, 472, 1272
- van de Sande, J., Kriek, M., Franx, M., et al. 2013, *ApJ*, 771, 85
- van der Wel, A., Franx, M., van Dokkum, P. G., et al. 2014, *ApJ*, 788, 28
- van der Wel, A., Rix, H.-W., Wuyts, S., et al. 2011, *ApJ*, 730, 38
- van Dokkum, P. G., Bezanson, R., van der Wel, A., et al. 2014, *ApJ*, 791, 45
- van Dokkum, P. G., Franx, M., Kriek, M., et al. 2008, *ApJL*, 677, L5
- van Dokkum, P. G., Nelson, E. J., Franx, M., et al. 2015, *ApJ*, 813, 23
- Vogelsberger, M., Genel, S., Springel, V., et al. 2014, *MNRAS*, 444, 1518
- Wake, D. A., van Dokkum, P. G., & Franx, M. 2012, *ApJL*, 751, L44
- Weiner, B. J., Willmer, C. N. A., Faber, S. M., et al. 2006, *ApJ*, 653, 1027
- Wellons, S., Torrey, P., Ma, C.-P., et al. 2015, *MNRAS*, 449, 361
- Wellons, S., Torrey, P., Ma, C.-P., et al. 2016, *MNRAS*, 456, 1030
- Whitaker, K. E., Franx, M., Leja, J., et al. 2014, *ApJ*, 795, 104
- Williams, C. C., Giavalisco, M., Cassata, P., et al. 2014, *ApJ*, 780, 1
- Wisnioski, E., Förster Schreiber, N. M., Wuyts, S., et al. 2015, *ApJ*, 799, 209
- Wuyts, S., Cox, T. J., Hayward, C. C., et al. 2010, *ApJ*, 722, 1666
- Wuyts, S., Förster Schreiber, N. M., Lutz, D., et al. 2011a, *ApJ*, 738, 106
- Wuyts, S., Förster Schreiber, N. M., van der Wel, A., et al. 2011b, *ApJ*, 742, 96
- Wuyts, S., Förster Schreiber, N. M., Wisnioski, E., et al. 2016, *ApJ*, 831, 149
- Yan, R., Newman, J. A., Faber, S. M., et al. 2006, *ApJ*, 648, 281
- Zolotov, A., Dekel, A., Mandelker, N., et al. 2015, *MNRAS*, 450, 2327